The fate of cells undergoing spontaneous DNA damage during development

Agnes Miermont[1,2], Vlatka Antolović[1,2], Tchern Lenn[1], John M.E. Nichols[1], Lindsey J. Millward[1] and Jonathan R. Chubb[1,3]

[1] MRC Laboratory for Molecular Cell Biology and Department of Cell and Developmental Biology, University College London, Gower Street, London, WC1E 6BT, London

[2] Equal Contributions

[3] Correspondence to: j.chubb@ucl.ac.uk

Summary: a combination of single cell transcriptomics and live cell imaging reveals multiple mechanisms by which cells experiencing spontaneous DNA damage are marginalised from normal development.

Development • Accepted manuscript

Abstract

Embryonic development involves extensive and often rapid cell proliferation. An unavoidable side effect of cell proliferation is DNA damage. The consequences of spontaneous DNA damage during development are not clear. Here we define an approach to determine the effects of DNA damage on cell fate choice. Using single cell transcriptomics, we identified a sub-population of *Dictyostelium* cells experiencing spontaneous DNA damage. Damaged cells displayed high expression of *rad51*, with the gene induced by multiple types of genotoxic stress. Using live imaging, we tracked high Rad51 cells from differentiation onset until cell fate assignment. High Rad51 cells were shed from multicellular structures, excluding damaged cells from the spore population. Cell shedding resulted from impaired cell motility and defective cell-cell adhesion, with damaged cells additionally defective in activation of spore gene expression. These data indicate DNA damage is not insulated from other aspects of cell physiology during development and multiple features of damaged cells prevent propagation of genetic error. Our approach is generally applicable for monitoring rare sub-populations during development, and permits analysis of developmental perturbations occurring within a physiological dynamic range.

Introduction

An inevitable consequence of the extensive cell proliferation occurring during embryonic development is that cells will suffer spontaneous DNA damage. Although many causes of DNA damage are associated with external factors, a large proportion of damage is incidental to normal cell metabolism and physiology (Lindahl and Barnes, 2000). Despite the high frequency at which spontaneous DNA damage occurs, we have very limited understanding of how cells react to this stress during development.

Most studies of DNA damage responses (DDRs) are carried out using treatments of large doses of a DNA damaging agent. Although highly useful for understanding the biochemistry of induced DDRs, these extreme treatments do not reveal how cells normally deal with spontaneous DNA damage in a developmental context. Characterisation of spontaneous DDRs is complicated because the lack of synchronicity of damage between cells masks the cell response (Karanam et al., 2012; Uphoff et al., 2016). As a result, it is unclear to what extent cell fate choice is insulated from the effects of DNA damage. Are cells repaired and reintegrated? Alternatively, are they excluded or marginalized from normal development?

To determine the effects of spontaneous DNA damage during development requires the ability to identify and then follow the damaged cells in tissues. Identification of specific cell states in complex differentiating tissues can be achieved using single cell transcriptomics (Briggs et al., 2018; Farrell et al., 2018; Wagner et al., 2018). These methods provide a snapshot in time of the cell state, but they cannot follow a single cell over time. To understand how a specific cell will behave during development also requires live cell imaging, to directly monitor developmental outcome of the cell in question (Meyer et al., 2017; Pelaez et al., 2015).

In this study, we have determined the fates of cells undergoing spontaneous DNA damage, by combining single cell transcriptomics with long term live imaging of single cells during the development of *Dictyostelium.* We have identified a sub-population of undifferentiated cells undergoing spontaneous DNA damage. Tracking the damaged cells during differentiation revealed the cells are shed from the rear of the migrating multicellular phase. Contributions to this shedding phenotype come from an impairment in cell motility and a strong cell-cell adhesion defect displayed by the damaged cells. Damaged cells also show impaired induction of spore-specific gene expression. This work demonstrates a combination of approaches to test the effects of cellular stress on developmental processes, and reveals multiple mechanisms by which development can exclude cells that are undesirable to propagate to the next generation.

Results

Populations of apparently equivalent cells can show a tremendous amount of variability in gene expression, suggesting hidden sub-populations of cells with different phenotypic states (Symmons and Raj, 2016). To reveal potential sub-populations, we analysed single cell transcriptome data of undifferentiated *Dictyostelium* cells (Antolovic et al., 2017) to identify genes expressed with a high level of variability. Data were plotted to reveal the variability in the expression of each gene (Fig. 1A). The horizontal axis (expression) represents normalised read counts. The vertical axis shows a measure of variance (the squared coefficient of variation, CV^2). Each gene is a dot. The red line is a running median through the data, with genes above the line more variable than average, and genes below the line (such as *act5*) less variable than average. One of the most variably expressed genes was *rad51*, which encodes a conserved eukaryotic protein required for the repair of double strand breaks by homologous recombination (Chapman et al., 2012).

To test whether variable expression could be detected at the protein level, we generated a knock-in cell line, with the fast-folding fluorescent protein, mNeonGreen (Neon) (Shaner et al., 2013) inserted at the 3' end of the *rad51* coding sequence. Although *Dictyostelium* are haploid, the parental strain has a duplication of the chromosomal region containing the *rad51* gene, which allows tagging of one locus while leaving the other for normal physiological function. Expression of the Rad51-Neon reporter was highly variable, with a rare (<1%) population of cells showing strong nuclear staining and the remainder of the population showing only weak basal expression (Fig. 1B). This variable expression contrasted the more uniform expression of an *act5* (actin) knock-in reporter. These expression properties of Rad51 were also demonstrated using flow cytometry (Fig. 1C). Most cells had higher fluorescence than parental cells, indicating weak basal expression in the bulk of the population, and a few cells had very high Rad51 expression. This distinctive variability implies heterogeneous Rad51 expression marks specific sub-populations of undifferentiated cells.

What underlying cell state does high Rad51 represent? Rad51 is required for repair of DNA double strand breaks (DSBs) (Chapman et al., 2012), and also assists in repairing other types of DNA damage (Carr and Lambert, 2013). We therefore suspected cells with high Rad51 reporter expression were undergoing spontaneous

DNA damage. To test this, we stained Rad51-Neon cells with an antibody against phospho-H2AX, a DNA damage marker (Fig. 2A and S1 A,B). This revealed a good correlation (r = 0.63, average from 3 replicates), implying considerable overlap between the high Rad51 state and DNA damage. We then tested whether high Rad51 cells are undergoing DNA damage by measuring correlations between expression of *rad51* and other genes linked to DNA damage, from single cell transcriptomic data from undifferentiated cells. *Rad51* was strongly correlated in its expression to many other DNA damage response genes (Fig. 2B). Additionally, we searched for all transcripts correlated with *rad51* at r > 0.5. Of the 30 genes identified by these criteria (Table S1), 25 are directly involved in DNA repair or replication. Similar to *rad51,* we found that most GO-annotated DNA repair genes are more variable than the transcriptome average (Fig. S1C).

The transcripts correlated with *rad51*, categorised by the types of damage they respond to, are not related to a single repair process (Fig. 2B, Table S1). For example, correlated transcripts include *adprt2* and *adprt1a* (non-homologous end-joining), *apeA* (base excision repair), *rad50* (DSB repair) and *rnrA* (replication stress), suggesting *rad51* can be induced by multiple forms of DNA damage. In support of this idea, treatment of Rad51-Neon cells with several different DNA damaging agents strongly induces reporter expression (Fig. 2C). *Dictyostelium* has been previously shown to be strongly resistant to different types of DNA damage (Hsu et al., 2006; Hudson et al., 2005; Zhang et al., 2009), so we used high doses for most agents. We observed the strongest Rad51 induction by hydroxurea (HU) and Camptothecin (CPT), which impair de novo dNTP synthesis and Topo I, respectively. Cisplatin (DNA crosslinker) and MMS (methylates DNA) also showed clear effects. Mitomycin C (DNA crosslinker) and Etoposide (inhibits Topo II) elicited weak effects, as did bleomycin (DSBs). Although bleomycin induced strong Rad51 expression at 300mU (Fig. S1D), this is two orders of magnitude more bleomycin than required for cell cycle arrest in *Dictyostelium* (Muramoto and Chubb, 2008). It was surprising that an agent causing DSBs only weakly induced a molecule central to DSB repair. However, as basal Rad51 is expressed in all cells, this basal level may be sufficient to deal with incidental DSBs, with high Rad51 induction required to assist responses to other forms of genotoxic stress. In summary, we propose the high Rad51 state represents a broad response to multiple types of DNA damage.

Dynamics of Rad51 expression

To determine how long the high Rad51 state persists for, we flow-sorted high and low Rad51-Neon cells, then monitored the fluorescence of cells at different times after sorting. More than 50% of the high-sorted cells were still classed as high one day post-sorting (Fig. S2A,B). This proportion continued to fall, and by 6 days, was close to the starting value of the unsorted population. Surprisingly, a small proportion of the low-sorted population induced Rad51 during the post-sort recovery. We interpret this as an effect of the sorting process, perhaps caused by DNA damage in response to mechanical stress (Raab et al., 2016) or cross-protection between stress-response pathways (Yaakov et al., 2017). The average long-term clonal recovery of sorted high Rad51 cells was not impaired, although recovery was more variable (Fig. S2C). The developmental morphology of the sorted high and low Rad51 cells was also similar (Fig. S2D). Together, these data indicate that the high Rad51 cells revert to basal Rad51 within a few days, and have no clear long-term viability phenotype.

To gain insight into the Rad51 induction process, we carried out long-term time lapse imaging of Rad51-Neon cells. For long-term tracking of rare events in populations of motile cells it was necessary to image several thousand cells to obtain 21 clear *rad51* induction profiles. We observed three classes of Rad51 induction profile, plotted as intensity time series in Fig. 2D and Fig. S3. In the first example (Fig. 2D, left) related cells show correlated induction. The initial cell (purple) showed a modest increase in overall fluorescence before dividing, after which the fluorescence falls. The two daughters (blue and pink) showed only small increases. In the granddaughter generation, both progeny of the pink cell (red) showed a strong Rad51 induction. In this lineage, Rad51 expression plateaued after 3-4h, remaining high in both granddaughters, which failed to divide before the end of the movie. In contrast, other sister pairs showed uncorrelated Rad51 induction (Fig. 2D, centre). One daughter (pink) rapidly induced and took a long time to divide, while the other daughter divided rapidly without Rad51 induction. Overall, 8/21 of the lineages traced showed correlated induction and 8/21 showed uncorrelated induction. Of the remaining cells, 3 could not be unambiguously classified and 2 showed a different behaviour (Fig. 2D, right), where sisters were correlated, but the increase in one sister was deferred a generation. Correlated increases may result from damage to the mother cell, with the

damage passed to both daughters. Uncorrelated increases imply damage specific to one daughter only. Deferred increases possibly suggest a metastable feature of the cell state that enhances the probability of a substantial damage event. Again, these studies imply different forms of DNA damage can give rise to the high Rad51 state.

Other features of the response to spontaneous DNA damage emerged from lineage analysis. Firstly, the cell cycles of damaged cells have longer duration than those with low *rad51* expression (Fig. 2E). The correlation of *rad51* expression and cycle time is modest (r=0.37, averaged over 4 experiments), contrasting standard DNA damage studies involving experimental administration of genotoxic stress, where sharp population-wide arrest occurs. The correlation we observed may reflect a lower bound estimate, as imaging windows bias against capture of longer duration events. Secondly, although their cycles tended to last longer, we observed 10 divisions of high Rad51 cells (Fig. 2D, S3). In 9/10 cases, the high Rad51 cells divided their fluorescence roughly equally between the daughters, without daughters approaching the levels of the initial induction. Only a single damaged cell (Fig. 2D, centre) had progeny with Rad51 re-induction to the same level as the parental cell. This implies that in cells that divide, the damage response usually begins to decay upon completion of the cell cycle. Finally, the mean time of induction of Rad51-Neon (defined as when daughter intensity exceeds the pre-mitotic value) is 126 minutes post-mitosis, with a low variability (SD = 48). This timing might be explained if Rad51 induction is triggered by detection of DNA damage by the cell during S-phase, which occurs immediately after mitosis in *Dictyostelium* (Weijer et al., 1984).

To further investigate the cell cycle disruption occurring in response to spontaneous DNA damage, we expressed mCherry-PCNA in Rad51-Neon cells (Fig. S4A). During mitosis, PCNA distributes through the cell as the nuclear envelope perforates, then rapidly binds to the separated chromatids as nuclei reform (arrows)(Muramoto and Chubb, 2008; Stevense et al., 2010). With no G1, DNA replication begins immediately after mitosis. 20 minutes into the new cell cycle, PCNA is enriched at heterochromatin (late S-phase; arrowheads). Comparing high and low Rad51 cells showed effects on multiple cycle phases (Fig. S4B). Mitosis was longer (p = 0.0014) and early S-phase shorter (p < 0.0001) in high Rad51 cells, with late S-phase not significantly altered (p = 0.073). Differences were slight, indicating most of the increase in cycle duration in high Rad51 cells is explained by an extended G2. We observed no

obvious disruption of the characteristic S-phase PCNA morphology in high Rad51 cells, after or prior to Rad51 induction. During the cell cycle in which Rad51 was induced, but prior to induction, we observed durations of mitosis, early and late S-phase similar to basal Rad51 expressers (Fig. S4B).

Fate of cells undergoing spontaneous DNA damage

Upon starvation, *Dictyostelium* cells undergo a simple differentiation programme, where individual cells aggregate together into a multicellular mound, before differentiating into two major cell types- stalk and spore (Williams, 2006). To determine the fate of the high Rad51 cells during development, we imaged cells from the start of differentiation until after the mound stage, when fate could be ascertained. Imaging large fields of view allowed tracking cells during the rapid motility and chemotaxis underlying aggregation. We imaged Rad51-Neon cells from the onset of development, until slug formation (Fig. 3A; Movies 1, 2), which occurs after cells decide their fates (Thompson et al., 2004). Early in development, cells are relatively stationary. As pulsatile extracellular cAMP signalling begins, cells undergo large-scale chemotaxis into streams, which merge into mounds. Most high Rad51 cells underwent chemotaxis into streams, indicating they differentiated to aggregation competence. The expression of Rad51-Neon remained relatively stable during the chemotaxis phase (Fig. S5A). Most high Rad51 cells engaged with mounds, however by the end of aggregation, many of the brighter cells resided at mound edges (Fig. 3A and B).

To quantify this edge recruitment, mounds were divided into two concentric regions of equal area (Fig. 3C). We found that the high Rad51 cells were enriched more in the outer region, than the inner one contrasting the more uniform distribution of cells expressing Neon or GFP from an endogenous actin (*act5*) promoter (Fig. 3D)(p = 4.7 x 10^{-7} and 6.1 x 10^{-10} respectively). The position of high Rad51 cells can be dynamic, with some cells switching between outside and centre (Fig. 3E)

What is the fate of the high Rad51 cells as development proceeds further? To address this, we imaged the distribution of high expressing cells as the aggregates become motile (the slug phase). In many slugs, there was a strong enrichment of high Rad51 cells at the rear (Fig. 4A and S5B). To quantify this, slug images were divided into 4 equal areas, from anterior to posterior (Fig. 4B). The control was 1% *act5*-Neon cells mixed with unlabelled wild-types, which showed no strong bias towards specific

slug regions (Fig. 4C, right panel, and Fig. S5B). For identifying Rad51-Neon cells, which, unlike *act5,* have a highly variable expression level, we used a multiple threshold approach, to avoid user biases in identifying a cell as either high or low. We scored the frequency of high cells in each area, by considering multiple thresholds for what constitutes a bright cell. At low thresholds, where more cells are considered "bright", the slugs had a more uniform distribution of Rad51, with slight enrichment at the front and rear. At higher thresholds, where fewer cells are "bright", the distribution of the cells was more enriched at the rear (Fig. 4C). This indicates that the higher the Rad51-Neon expression, the greater its rear tendency. It initially seemed possible that the rear-localisation of high Rad51-Neon cells might be caused by some emergent effect of a C-terminal fusion of Neon to Rad51. To test this possibility, we inserted Neon at the 5' end of the Rad51 locus, with a series of STOP codons and a selectable marker before the Rad51 coding sequence (*rad51*-Neon[GR]). Cells expressing high levels of this Neon reporter were also localised to the rear of slugs, indicating that the localisation of high Rad51-Neon cells was not an effect of the fusion of Rad51 to a reporter (Fig. 4C; middle panel).

Many slugs showed a trail containing bright Rad51-Neon cells, suggesting slugs were losing bright cells at their rear. This suggestion was confirmed by live imaging of the multicellular phases of development (Fig. 4D and Movies 3 and 4). Fig. 4D shows a mound as it converts into a slug. The high Rad51 cells initially engaged with the mound, often internal to it, and in some cases are highly migratory within the structure (red arrow). However, as the structure begins to migrate away, almost all the bright cells are left behind.

The shedding of high Rad51 cells means they are less likely to become spores, and images of fruiting bodies show no high Rad51 cells in the spore head (Fig. 4E) although a few remain in stalk lineages, such as in the lower cup and basal disc area, perhaps reflecting the partial enrichment in the anterior zone of the slug (Fig. 4C), from which stalk cells are derived. The relative abundance of the high Rad51 cells was reminiscent of Sentinels, the *Dictyostelium* immune-like cells (Chen et al., 2007). However, we found no correlation between Rad51-Neon expression and ethidium bromide uptake, which marks Sentinels, in either intact slugs or dissociated cells (Fig. S5 C,D).

Impaired motility and cell-cell adhesion of high Rad51 cells

What features of the high Rad51 cells cause them to detach from aggregates? The high Rad51 cells display a slightly increased cell volume (Fig. 5A). The overall correlation between volume and Rad51 expression is weak, however the great majority of the brightest 1% of cells are larger than average. This may be caused by the extended cell cycles and a slightly increased frequency of multinucleate cells in the high Rad51 population (high rad51: 29±3%; low 15±8%; 3 replicates). An increase in cell size may alter the physical ability of a cell to enter and move within multicellular structures. It may also have different adhesive properties, and potentially different amounts of signalling receptors on its surface.

To test the potential effects of an increase in cell size on cell fate, we monitored the developmental behaviour of diploid strains mixed into haploids. *Dictyostelium* cells are normally haploid, but can form stable diploids. Diploid cells develop robustly (King and Insall, 2003) and are slightly larger than haploids (Fig. S6A). Can this increased size drive cell shedding? When diploids (labelled with Neon and mScarlet) were mixed into haploid slugs (labelled with Neon), we found the opposite (Fig. 5B and C). Diploids were not shed from the rear of slugs in significant numbers, and instead were slightly enriched at the slug anterior. Although this anterior distribution may also relate to diploid-specific features, it does not provide evidence that increased cell size causes cell shedding.

Cells are highly motile in the mound and slug, with centre of the mound and anterior of the slug acting as chemotactic signalling centres (Weijer, 2004). A defect in chemotaxis or cell motility would impair the ability of a cell to migrate to the centre of the mound, or anterior of a slug. Are chemotaxis and motility phenotypes associated with the high Rad51 state? To test this, we imaged Rad51-Neon cells during chemotactic aggregation and measured the speed and directionality of high and low Rad51 cells (Fig. S6B). The directionality of the high Rad51 cells was not significantly perturbed (Fig. 5D), however, we found a reduction of cell speed in the high Rad51 state (Fig. 5E). Closer analysis of single cell behaviours during chemotaxis revealed most high Rad51 cells had normal cell speeds, but a significant minority were nearly immobile (Fig. 5F). These measurements were taken on cells before they entered the multicellular structures, however, similar behaviours were clearly identified in multicellular aggregates (Fig. 4D, Movie 3,4) with some cells retaining high motility

before being shed, and others appearing static throughout the movie. In general, the multicellular environment is likely to place a greater obstacle to cell motility, potentially exacerbating this partially penetrant effect on motility observed in isolated cells.

Forming and maintaining the multicellular stages also requires cell-cell adhesion (Loomis, 2015). Could an adhesion defect contribute to the shedding of the high Rad51 cells? There was no clear signature in our single cell transcriptomic data that cells with DNA damage have impaired regulation of adhesion genes. Fig. S6C shows the correlations, in mound stage expression data (Antolovic et al., 2019) between *rad51* and transcripts of genes with annotated roles in adhesion. No transcripts showed strong positive or negative correlations with *rad51*. To more directly test the possibility that high Rad51 cells have defective adhesion, we used a cell re-aggregation assay (Xu et al., 1996)(Fig. 6A). Mounds were disaggregated to single cells, then images captured to allow an initial cell count and to establish the signal intensity corresponding to a 1% intensity threshold. For robust thresholding we counted around 7500 cells per replicate. The cells were then allowed to adhere to each other. The null hypothesis was that the high Rad51 cells would aggregate in proportion to their overall fraction of the population. If true, we would expect 1% of the non-aggregated population would be high Rad51. We tested for both divalent cation-dependent and independent adhesion effects. In the presence of divalent cations (Mg^{2+} and Ca^{2+}), high Rad51 cells were strongly enriched in the non-adherent pool, compared to the expected 1% null value (χ^2 test: $p < 0.0001$; Fig. 6B). The scale of this effect indicates the high Rad51 cells are over 5 fold more likely to remain non-adherent than low Rad51 cells (Fig. S7). In contrast, without divalent cations (EDTA), where adhesion is much weaker, the high Rad51 cells showed a similar ability to adhere as the rest of the population. We conclude that the high rad51 cells show a divalent cation-dependent adhesion defect.

Impaired prespore marker induction in high Rad51 cells

Is the lack of high Rad51 cells in the spore population solely because reduced adhesion and motility give rise to shedding, or are high Rad51 cells additionally blocked from entering the spore differentiation pathway? To test this possibility, we transformed Rad51-Neon cells with an extrachromosomal plasmid expressing mCherry under the control of the promoter of the prespore gene *pspA.* The transformed cells were developed to the mound stage, disaggregated and the fluorescence levels of individual

cells measured using flow cytometry. Flow plots for control Rad51-Neon cells are shown in Fig. 6C and S8A. The plots for Rad51-Neon cells transformed with the *pspA*-mCherry vector show a strong induction of red fluorescence, however, this is only in the low Neon fluorescence part of the spectrum (Fig. 6D). Using a 1% cut off to separate high and low Rad51 Neon cells shows that the high cells barely induce this prespore marker (χ^2 test: p < 0.00001; Fig. 6E). This implies the high Rad51 cells have a spore differentiation block, in addition to motility and adhesion effects on cell retention in aggregates. Analysis of mound single cell transcriptomic data (Antolovic et al., 2019) does not provide clear indications why high Rad51 cells fail to differentiate as spores. Rare cells expressing high levels of *rad51* mRNA can be identified in mound cells prior to fate separation (arrow Fig. S8B), consistent with the idea that damaged cells can adopt a temporally normal mound expression state.

Discussion

Using a combination of single cell gene expression methods, we have identified a sub-population of undifferentiated *Dictyostelium* cells undergoing spontaneous DNA damage, marked by high levels of Rad51 expression. Several lines of evidence suggest multiple forms of damage can cause the high Rad51 state. The long-term viability of high Rad51 cells was not strongly impaired, although short-term increases in cell cycle duration were detected. We tracked the high *rad51* expressing cells from the onset of development through to the multicellular stages of development, and observed that these cells are preferentially shed from multicellular structures. The shedding of the damaged cells was associated with reduced motility and adhesion, which are likely to impair the ability of cells to remain within the multicellular aggregate. In addition, the damaged cells have a strong impairment in the induction of gene expression associated with spore differentiation. These features of the damaged cells combine to prevent the cells contributing their genetic material to the next generation of cells.

What happens to the cells after they are shed? Although excluded from the fruiting body, discarded cells have the potential to dedifferentiate on bacterial food sources, then re-enter the developmental programme within a few days (Kuzdzal-Fick et al., 2007). This may provide an option to the organism for local geographical expansion, by throwing away damaged cells, giving them a chance of survival, whilst at the same time protecting the integrity of the spore population. Not all the discarded cells had high Rad51, suggesting shedding also occurs in response to other forms of stress. Consistent with this idea, mutants of *Dictyostelium* with defective fat metabolism also fail to efficiently enter the spore population (Kornke and Maniak, 2017).

The effects of DNA damage are not insulated from several aspects of cell physiology, with a loss of spore generating potential linked to multiple causes. A possible cause of the impairment in the spore differentiation response may originate from the regulation of the cell cycle. In the late mound and early slug, prespore cells undergo a wave of cell division (Zimmerman and Weijer, 1993). Any process, such as DNA damage, which delays or otherwise interferes with cell cycle progression, might impair the development of the spore fate.

We expect that the combination of approaches we implemented here will be directly applicable to investigating the response to spontaneous DNA damage in more complex developmental systems. Many DDR proteins were heterogeneously expressed,

and like Rad51, many of these proteins are conserved throughout eukaryotes, providing a rich set of candidates for investigation.

More generally, our approach is suitable for studying the behaviour of rare cell populations in complex tissues, for example in the study of lineage priming, or other forms of stress, such as in cell competition. The ability to directly visualise the behaviour of a natural perturbation, rather than an experimental treatment, gives an improved physiological context for understanding how cells manage stimuli during development, in their normal niche, within the physiological range of stimuli, with a realistic level and balance in the activation of the many cell response pathways. By identifying markers of the natural response, and following these markers over time until fate can be ascertained, we can approach a more meaningful understanding of the dynamics and regulation of tissue composition during development.

Materials and Methods

Cell handling

Dictyostelium cells were cultured at 22°C in HL5 medium (Formedium) or on SM agar plates with *Klebsiella* lawns as a nutrient source. Cell lines were validated by Southern blotting and PCR, and maintained using selection against bacteria in HL5 media (Formedium). Cells never exceeded confluence and were discarded after 10 days of culture. For development, cells were resuspended in KK2 buffer (20 mM KPO_4, pH 6.2) and deposited on 1.5% non-nutrient agar in KK2, at a density of 3.5 x 10^5 cells/cm^2. After allowing cells to settle, KK2 was removed and cells were incubated in a humid box (22°C). Diploids were generated as described (King and Insall, 2003), combining AX3 cells expressing either mNeonGreen (blasticidin resistant) or mScarlet (hygromycin resistant (Paschke et al., 2018)) from the *act5* locus (Muramoto et al., 2012). After 10-14 days selection in blasticidin and hygromycin, the culture containing only double resistant/double fluorescent cells was expanded and used directly. For labelling Sentinel cells, 3μg/ml Ethidium Bromide was added to the agar, with multicellular structures disaggregated, when required, by passing them 15 times through a 23G needle. For inducing DNA damage, we used overnight treatments of Bleomycin sulfate (Sigma B1141000), Camptothecin (CPT) (Sigma C9911), Etoposide (Sigma E1383), Hydroxyurea (Sigma H8627), Mitomycin C (MMC) (Sigma M0503), Cisplatin (Sigma C2210000) and Methyl methanesulfonate (MMS) (Sigma 129925).

Cell-sorting was performed at the UCL GOS ICH Flow Cytometry Core Facility using a MoFlo XDP running IntelliSort software. Flow cytometry used a BD LSR II cell analyser running BD FACS Diva Software v6.1.3 (BD Biosciences). FlowJo software was used for data analysis and graphic rendering.

Generation of recombinant cell lines

We generated a fluorescent Rad51 reporter cell line by targeting a *Dictyostelium* codon-optimised sequence encoding mNeonGreen (Neon)(Tunnacliffe et al., 2018) at the 3' end of the *rad51* coding sequence, generating an in frame Rad51-Neon fusion. We used AX3 cells and for cell tracking, we used AX3 cells previously engineered to express a red fluorescent nuclear marker (H2Bv3-mCherry)(Corrigan and Chubb, 2014). The

targeting vector contained a left homology arm spanning nucleotide 1276 to 2232 of the *rad51* genomic sequence (Basu et al., 2015) (TAA is at 2233). Following this was a linker encoding GPVQRS, followed by Neon. After the STOP codon of Neon followed the blasticidin resistance cassette, then the right homology arm, spanning from 2193 to 2686. Single copy insertions of the correct size were confirmed by Southern blots. To generate the gene replacement Rad51-Neon cell line (*rad51*-Neon[GR]), the left homology arm spanned the promoter (406-1021) and the right arm spanned 1115-1998 of the *rad51* genomic sequence. For this vector, Neon is preceded by the first 7 amino acids of *rad51* and the HindIII encoded linker, CT. The *pspA*-mCherry expression vector was derived by cloning a -538 to +27 fragment (+1 is the A of ATG) containing the promoter and initial codons of *pspA* upstream of mCherry in extra-chromosomal vector pDM1097.

Imaging

For immunostaining with anti-phospho-H2A.X, cells were stained with primary antibody against Phospho-Histone H2A.X (Ser139) (Cell Signaling 9718). For cell volume measurements, we used a Leica SP8 confocal. Rad51-Neon cells were stained with FM 4-64. Excitation used a white light laser (3.4% power) at 495 nm for both channels with emission windows 510-553 nm for Neon and 586-709 for FM 4-64, using HyD detectors. For diploid/haploid size measurements, we used the total cell fluorescence of mNeonGreen and mScarlet signals. For all size measurements, the pinhole was 65.3 microns (approx. 1 AU at 580 nm). Voxel dimensions were 569 nm x 569 nm x 349 nm (z axis).

For imaging of multicellular development stages, cells were developed on KK2 agar. Prior to imaging, 1 cm^2 squares of agar were excised, then inverted onto Delta TPG imaging dishes (Bioptechs) and covered in mineral oil to prevent drying. Slugs were imaged, as 100 μm 3D stacks, on an inverted Zeiss epifluorescence microscope (Muramoto and Chubb, 2008) using a 25x multi-immersion objective. Mounds were imaged on the Vox, using a 20x objective, also as 3D stacks.

For live imaging of the transition from the unicellular feeding stage to multicellular aggregation and slug migration, we plated cells in KK2 buffer on a thin layer of 1.5% agar in Nunc 2-well coverglass dishes. Excess buffer was removed, and the dish was wrapped in a thin layer of damp towel and sealed with parafilm. Imaging used the Vox, using a 10x air objective, a 5 minute capture interval, and 8 slice 3D stack

with a 10.63 μm Z-step.   Laser powers and exposure times were optimised to minimise photo damage. For imaging the dynamics of cell motility during aggregation, we imaged starving cells under non-nutrient agar using epifluorescence, using a 25x oil objective, at 40 s intervals.

For imaging the long-term cell-cycle dynamics of cells, cells were grown for 2 days in KK2/*Klebsiella* (OD10) in suspension, then plated with fresh *Klebsiella* (OD10) in 2-well dishes. 3D epifluorescence stacks were recorded on a Nikon N-STORM microscope, using a 20X DIC air objective and Andor Zyla camera, with a z-step size of 0.7 μm, every 5 minutes for 28-30 h. For imaging the dynamics of cell cycle phases, we expressed mCherry-PCNA using an extrachromosomal vector in the Rad51-Neon cells. Cells were imaged on an Olympus IX73 inverted epifluorescence microscope, using a Photometrics 95B Prime camera. 29 slice z-stacks were captured at multiple XY positions every 3 minutes, with red and green excitation from 565 nm and 470 nm OptoLEDs (Cairn Research) and a 1.4 NA 60x objective, for 50 ms per channel per z-slice.   Under these imaging conditions, we observed no induction of Rad51 by long term light exposure (Fig. S9).

Image analysis

For measuring cell intensities during cell growth and aggregation, we used the ImageJ plug-in "Time Series Analyzer v3". Cells were tracked until they became attached to streams or mounds. Directionality was defined as the distance between start and end points of the path divided by the total path length. Unless otherwise stated, we specified a threshold, in advance of analysis, on cell intensities of isolated cells to classify the 1% brightest cells as "high Rad51" and the bottom 99% as "low Rad51".

For measuring cell positions within mounds, the mound border was drawn manually in ImageJ, then the area of the selection was calculated and divided into two equal concentric areas. The detection threshold for high and low Rad51 expressers was estimated by eye on one mound, then applied automatically to all mounds captured within the same experimental day. We then calculated the ratio of the number of bright cells in the outer area versus number of bright cells in the inner area.

For measuring the position of bright cells in slugs, we first stitched partial slugs together using the "Pairwise Stitching" ImageJ plug-in. The slug border was defined

manually on maximal projections of the raw 3D stacks, and the area of the selection was calculated in ImageJ. The slug area was then divided into four equal parts, from anterior to posterior, and the number of high-expressing cells counted in each quarter. For control slugs (*act5*-Neon cells mixed 1:99 with wild-type cells) and haploid/diploid mixes, the high-expressing cells were identified using a manually determined threshold, as there was a clear and relatively homogeneous visual distinction between the expressing and non-expressing cells. For identifying Rad51- Neon and *rad51*-Neon[GR] cells, which have a highly variable expression level, we avoided user biases using a multiple threshold approach. We used a Particle Detection ImageJ plug-in (Sbalzarini and Koumoutsakos, 2005) with varying levels of threshold for particle detection and determined how the changing threshold affected the output distribution of bright cells. The range of thresholds was optimised to suit the reporter. For example, the *rad51*-Neon[GR] cells have fluorescence distributed uniformly around the cell, rather than concentrated in the nucleus, therefore required a lower range of detection thresholds to represent the data fairly. Unless stated otherwise, Mann-Whitney tests were used to assess the significance of differences between treatments.

For cell volume measurements we used Imaris (Bitplane, v7.6). We created surface objects from channel of interest using a standardised absolute threshold, manually determined for each experimental repeat. Surfaces touching the edge of the field of view were excluded, surfaces created by touching cells were manually split and object filters were applied to exclude cell fragments and large clumps of cells. For Rad51-mNeonGreen size measurements, we generated a binary membrane mask from surfaces made on FM 4-64 channel. The mask was exported to ImageJ where a custom plugin was used to fill in the cytoplasmic volume. This stack of binary images was then exported back into Imaris, where a new surface "object" was created for volume and intensity statistics to be measured.

Cell adhesion assays
Mounds were disaggregated to single cells in 1 ml KK2 + 15 mM EDTA by repeated passage through a 20G syringe. A 50μl sample of the single cell suspension was placed in an 8-well coverglass chamber containing 200 μl KK2 for counting (t=0). For adhesion, the remainder of the cells were resuspended in 1 ml KK2 with 1 mM $MgCl_2$ + 1 mM $CaCl_2$ or 1 ml KK2/15 mM EDTA in a 1.5 ml microcentrifuge tube, then shaken on

an orbital shaking incubator at 150 rpm. 100 μl was taken after 1h. Cells were imaged with a 10x objective on the Zeiss inverted microscope. 16 optical sections, centred in the z-axis on cell nuclei, were captured at 2 μm spacing for both Rad51-Neon and H2B-mCherry detection channels for up to 25 fields of view.

Image processing and quantification was automated in ImageJ. To quantify the Rad51-mNeon signal of each cell in a field of view, a sum z-projection was generated for each of the fluorescence channels. Nuclei were identified by finding maxima of the H2B-mCherry signal. A circular region of interest, centred on the maxima, with a 3.5 pixel radius was created. The sum of all green-channel pixel intensities in this region of interest was calculated.   For clustered samples, masks of single cells and 2-cell clusters in the field of view were first generated using brightfield images, based on a user-defined size threshold. The Rad51-mNeon signal was then obtained as above, using the H2B maxima, in the masked image. To determine the threshold intensity above which cells could be categorised as high-Rad51, t=0 cells were ranked by intensity and the 99th percentile intensity value used as the threshold.

References

Antolovic, V., Lenn, T., Miermont, A. and Chubb, J. R. (2019). Transition state dynamics during a stochastic fate choice. *Development* **in press**.

Antolovic, V., Miermont, A., Corrigan, A. M. and Chubb, J. R. (2017). Generation of Single-Cell Transcript Variability by Repression. *Current biology : CB* **27**, 1811-1817 e1813.

Basu, S., Fey, P., Jimenez-Morales, D., Dodson, R. J. and Chisholm, R. L. (2015). dictyBase 2015: Expanding data and annotations in a new software environment. *Genesis* **53**, 523-534.

Briggs, J. A., Weinreb, C., Wagner, D. E., Megason, S., Peshkin, L., Kirschner, M. W. and Klein, A. M. (2018). The dynamics of gene expression in vertebrate embryogenesis at single-cell resolution. *Science.*

Carr, A. M. and Lambert, S. (2013). Replication stress-induced genome instability: the dark side of replication maintenance by homologous recombination. *Journal of molecular biology* **425**, 4733-4744.

Chapman, J. R., Taylor, M. R. and Boulton, S. J. (2012). Playing the end game: DNA double-strand break repair pathway choice. *Molecular cell* **47**, 497-510.

Chen, G., Zhuchenko, O. and Kuspa, A. (2007). Immune-like phagocyte activity in the social amoeba. *Science* **317**, 678-681.

Corrigan, A. M. and Chubb, J. R. (2014). Regulation of transcriptional bursting by a naturally oscillating signal. *Current biology : CB* **24**, 205-211.

Farrell, J. A., Wang, Y., Riesenfeld, S. J., Shekhar, K., Regev, A. and Schier, A. F. (2018). Single-cell reconstruction of developmental trajectories during zebrafish embryogenesis. *Science.*

Hsu, D. W., Gaudet, P., Hudson, J. J., Pears, C. J. and Lakin, N. D. (2006). DNA damage signaling and repair in Dictyostelium discoideum. *Cell Cycle* **5**, 702-708.

Hudson, J. J., Hsu, D. W., Guo, K., Zhukovskaya, N., Liu, P. H., Williams, J. G., Pears, C. J. and Lakin, N. D. (2005). DNA-PKcs-dependent signaling of DNA damage in Dictyostelium discoideum. *Current biology : CB* **15**, 1880-1885.

Karanam, K., Kafri, R., Loewer, A. and Lahav, G. (2012). Quantitative live cell imaging reveals a gradual shift between DNA repair mechanisms and a maximal use of HR in mid S phase. *Molecular cell* **47**, 320-329.

King, J. and Insall, R. H. (2003). Parasexual genetics of Dictyostelium gene disruptions: identification of a ras pathway using diploids. *BMC genetics* **4**, 12.

Kornke, J. M. and Maniak, M. (2017). Fat-containing cells are eliminated during Dictyostelium development. *Biology open* **6**, 1294-1304.

Kuzdzal-Fick, J. J., Foster, K. R., Queller, D. C. and Strassmann, J. E. (2007). Exploiting new terrain: an advantage to sociality in the slime mold Dictyostelium discoideum. *Behavioral Ecology* **18**, 433-437.

Lindahl, T. and Barnes, D. E. (2000). Repair of endogenous DNA damage. *Cold Spring Harbor symposia on quantitative biology* **65**, 127-133.

Loomis, W. F. (2015). Genetic control of morphogenesis in Dictyostelium. *Developmental biology* **402**, 146-161.

Meyer, H. M., Teles, J., Formosa-Jordan, P., Refahi, Y., San-Bento, R., Ingram, G., Jonsson, H., Locke, J. C. and Roeder, A. H. (2017). Fluctuations of the transcription factor ATML1 generate the pattern of giant cells in the Arabidopsis sepal. *eLife* **6**.

Muramoto, T., Cannon, D., Gierlinski, M., Corrigan, A., Barton, G. J. and Chubb, J. R. (2012). Live imaging of nascent RNA dynamics reveals distinct types of transcriptional pulse regulation. *Proceedings of the National Academy of Sciences of the United States of America* **109**, 7350-7355.

Muramoto, T. and Chubb, J. R. (2008). Live imaging of the Dictyostelium cell cycle reveals widespread S phase during development, a G2 bias in spore differentiation and a premitotic checkpoint. *Development* **135**, 1647-1657.

Paschke, P., Knecht, D. A., Silale, A., Traynor, D., Williams, T. D., Thomason, P. A., Insall, R. H., Chubb, J. R., Kay, R. R. and Veltman, D. M. (2018). Rapid and efficient genetic engineering of both wild type and axenic strains of Dictyostelium discoideum. *PLoS One* **13**, e0196809.

Pelaez, N., Gavalda-Miralles, A., Wang, B., Navarro, H. T., Gudjonson, H., Rebay, I., Dinner, A. R., Katsaggelos, A. K., Amaral, L. A. and Carthew, R. W. (2015). Dynamics and heterogeneity of a fate determinant during transition towards cell differentiation. *eLife* **4**.

Raab, M., Gentili, M., de Belly, H., Thiam, H. R., Vargas, P., Jimenez, A. J., Lautenschlaeger, F., Voituriez, R., Lennon-Dumenil, A. M., Manel, N., et al. (2016). ESCRT III repairs nuclear envelope ruptures during cell migration to limit DNA damage and cell death. *Science* **352**, 359-362.

Sbalzarini, I. F. and Koumoutsakos, P. (2005). Feature point tracking and trajectory analysis for video imaging in cell biology. *Journal of structural biology* **151**, 182-195.

Shaner, N. C., Lambert, G. G., Chammas, A., Ni, Y., Cranfill, P. J., Baird, M. A., Sell, B. R., Allen, J. R., Day, R. N., Israelsson, M., et al. (2013). A bright monomeric green fluorescent protein derived from Branchiostoma lanceolatum. *Nature methods* **10**, 407-409.

Stevense, M., Muramoto, T., Muller, I. and Chubb, J. R. (2010). Digital nature of the immediate-early transcriptional response. *Development* **137**, 579-584.

Symmons, O. and Raj, A. (2016). What's Luck Got to Do with It: Single Cells, Multiple Fates, and Biological Nondeterminism. *Molecular cell* **62**, 788-802.

Thompson, C. R., Reichelt, S. and Kay, R. R. (2004). A demonstration of pattern formation without positional information in Dictyostelium. *Development, growth & differentiation* **46**, 363-369.

Tunnacliffe, E., Corrigan, A. M. and Chubb, J. R. (2018). Promoter-mediated diversification of transcriptional bursting dynamics following gene duplication. *Proceedings of the National Academy of Sciences of the United States of America* **115**, 8364-8369.

Uphoff, S., Lord, N. D., Okumus, B., Potvin-Trottier, L., Sherratt, D. J. and Paulsson, J. (2016). Stochastic activation of a DNA damage response causes cell-to-cell mutation rate variation. *Science* **351**, 1094-1097.

Wagner, D. E., Weinreb, C., Collins, Z. M., Briggs, J. A., Megason, S. G. and Klein, A. M. (2018). Single-cell mapping of gene expression landscapes and lineage in the zebrafish embryo. *Science*.

Weijer, C. J. (2004). Dictyostelium morphogenesis. *Current opinion in genetics & development* **14**, 392-398.

Weijer, C. J., Duschl, G. and David, C. N. (1984). A revision of the Dictyostelium discoideum cell cycle. *J Cell Sci* **70**, 111-131.

Williams, J. G. (2006). Transcriptional regulation of Dictyostelium pattern formation. *EMBO reports* **7**, 694-698.

Xu, X. S., Kuspa, A., Fuller, D., Loomis, W. F. and Knecht, D. A. (1996). Cell-cell adhesion prevents mutant cells lacking myosin II from penetrating aggregation streams of Dictyostelium. *Developmental biology* **175**, 218-226.

Yaakov, G., Lerner, D., Bentele, K., Steinberger, J. and Barkai, N. (2017). Coupling phenotypic persistence to DNA damage increases genetic diversity in severe stress. *Nature ecology & evolution* **1**, 16.

Zhang, X. Y., Langenick, J., Traynor, D., Babu, M. M., Kay, R. R. and Patel, K. J. (2009). Xpf and not the Fanconi anaemia proteins or Rev3 accounts for the extreme resistance to cisplatin in Dictyostelium discoideum. *PLoS Genet* **5**, e1000645.

Zimmerman, W. and Weijer, C. J. (1993). Analysis of cell cycle progression during the development of Dictyostelium and its relationship to differentiation. *Developmental biology* **160**, 178-185.

Figures
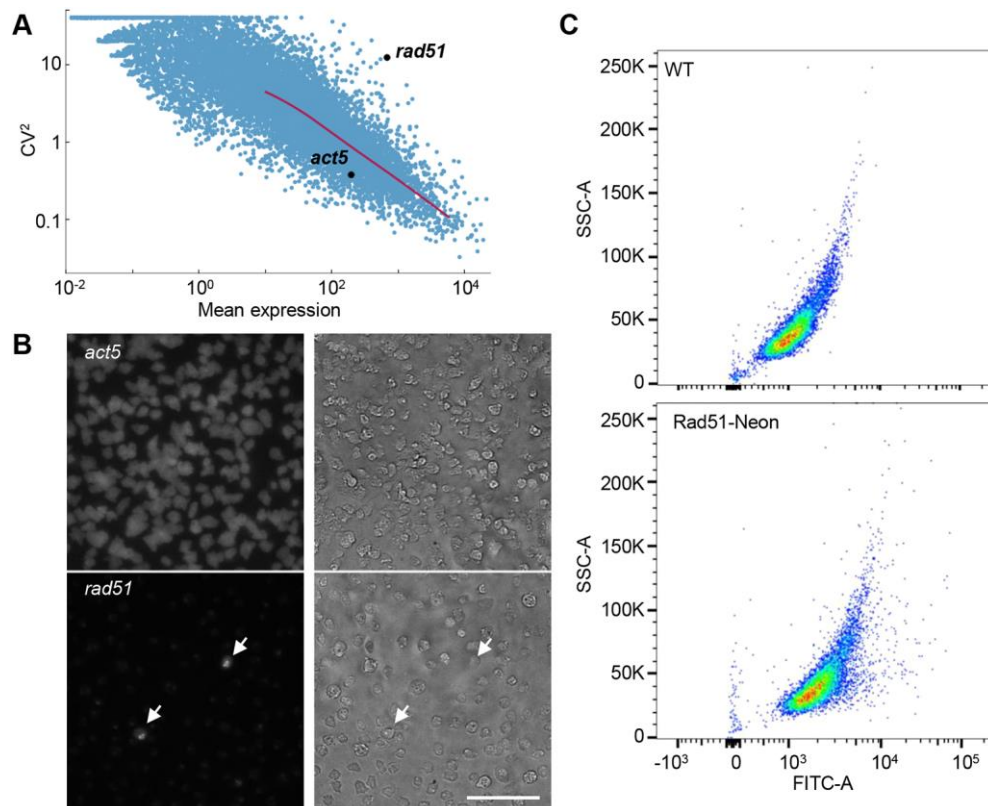
Fig. 1.

A high *rad51*-expressing sub-population of undifferentiated *Dictyostelium* cells.

A) Defining variably expressed genes by single cell RNA sequencing (scRNAseq). Plot shows the relationship between mean expression (read counts) and variability (CV^2 – the squared coefficient of variation) for genes in undifferentiated *Dictyostelium* cells. Each gene is represented as a dot. Genes above the median (red line) are more variable than average. Data from (Antolovic et al., 2017). B) Testing the variability in protein expression from the *rad51* gene. A C-terminal fusion of Rad51 to mNeonGreen (Neon), was generated by genome editing of the endogenous *rad51* locus and compared to a cell line with Neon coding sequence inserted in the *act5* gene. Adjacent bright-field images show all cells in fields-of-view. Scale bar 100µm C) Flow cytometry profiles of wild-type and Rad51-Neon knock-in cells. Horizontal axis (FITC-A) represents Neon fluorescence.
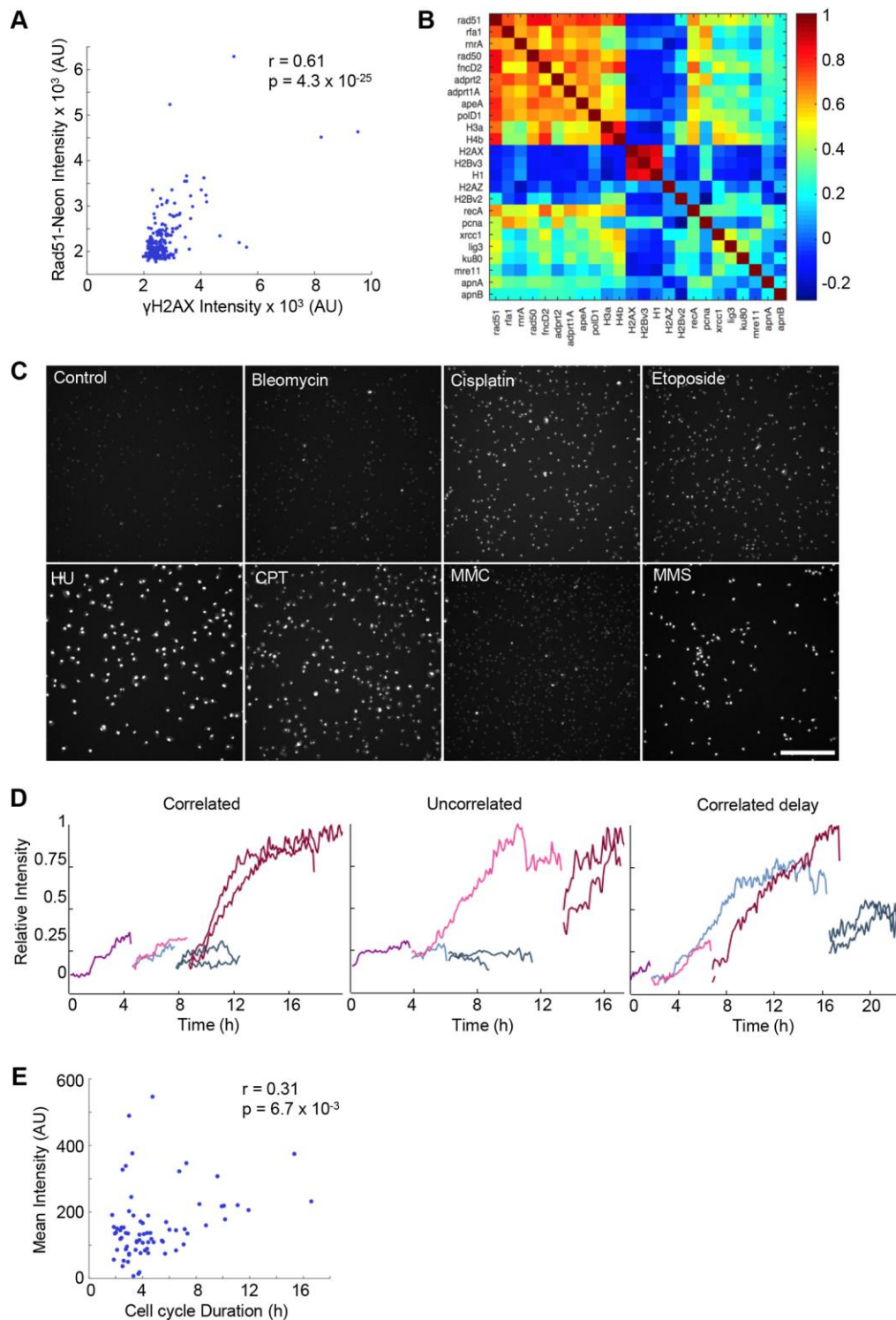
Fig. 2.

Regulation of *rad51* expression in undifferentiated *Dictyostelium* cells.

A) Rad51 expression is correlated with DNA damage. Single cell measurements of Rad51-Neon fluorescence compared to staining by an antibody for phosphorylated histone H2AX. The plot shows one experimental replicate (r = 0.61; p = 4.3 x 10^{-25}).

Additional replicates are shown in Fig. S1B. Average correlation for all 3 replicates: r = 0.63. B) Single cell correlations between *rad51* RNA expression and RNAs encoding other proteins associated with DNA repair. Correlation values were extracted from scRNAseq data on undifferentiated cells (Antolovic et al., 2017). C) Induction of Rad51-Neon using multiple genotoxic agents: 10 mU bleomycin, 300 μM cisplatin, 500 μM Etoposide, 30 mM HU, 10 μM CPT, 0.05 mg/ml MMC and 2.5 mM MMS. Scale bar is 100 μm. At least three independent experiments were carried out using microscope or flow cytometry, using multiple agent doses. D) Multiple cell generation time-lapse analysis of spontaneous Rad51-Neon induction. Individual panels show different types of intergenerational behaviour (see Fig. S3 for the complete dataset captured over 4 imaging experiments). In the left panel, after the second division, both daughter cells (red) induce Rad51-Neon strongly soon after the division. In the centre panel, one daughter (pink) strongly induces, whereas its sister does not induce. In the right panel, one daughter (blue) strongly induces, but its sister only induces strongly after it has divided (red). Traces have been smoothed with a sliding window of 2 frames (10 minutes). E) Correlation of Rad51-Neon intensity (cycle averaged) with cell cycle duration (r=0.31; p = 6.7 x 10^{-3}), showing one representative example of four independent experiments.
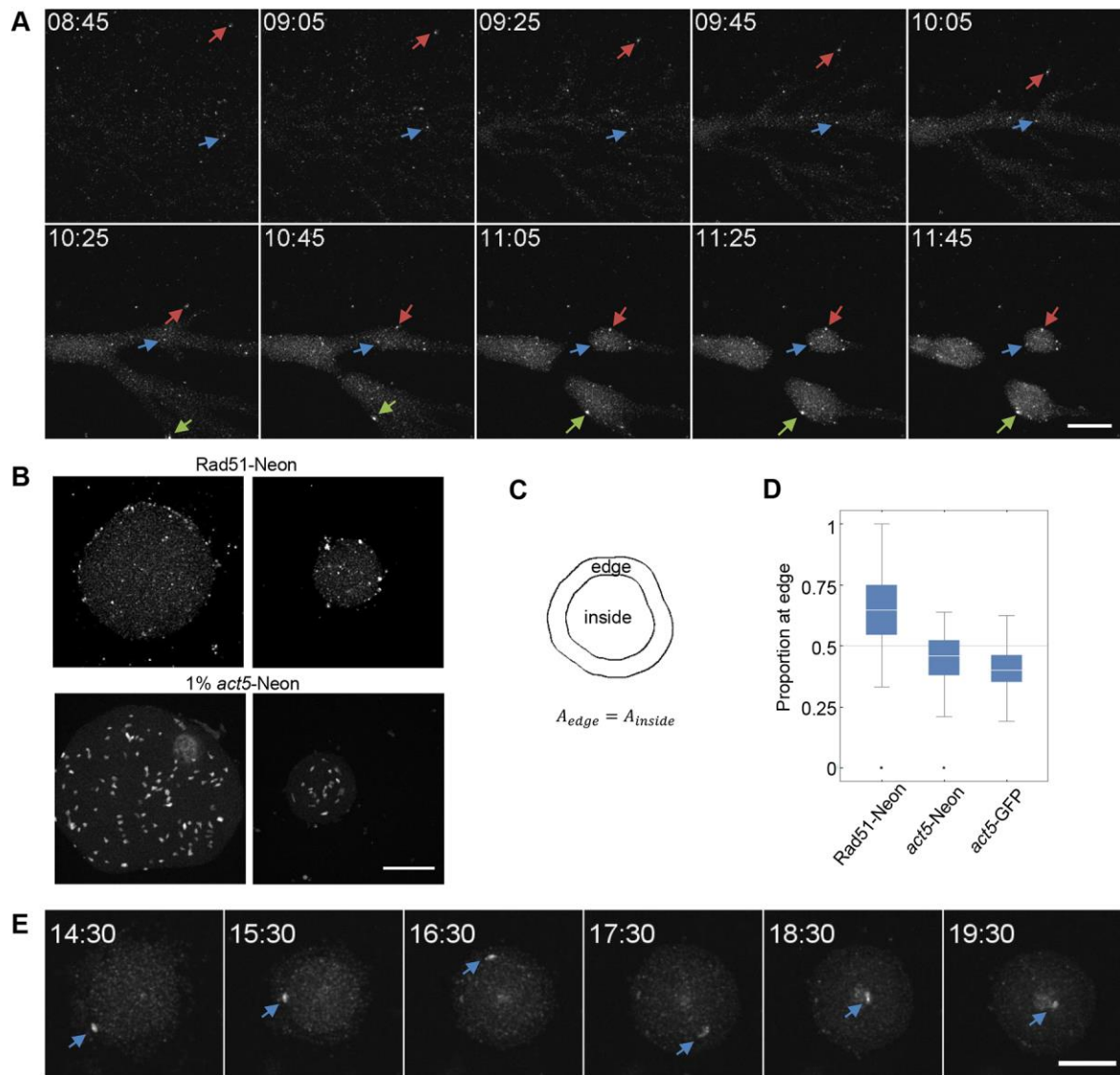
Fig. 3.

Effects of spontaneous DNA damage on cell fate

A) Time-lapse imaging of *Dictyostelium* aggregation showing the behaviour of cells with spontaneous DNA damage. High Rad51-Neon cells, such as those marked by arrows, can be tracked from the onset of differentiation, until late aggregation and slug departure. The high Rad51 cells remain at the edge of cell aggregates. Scale bar 150 μm. Maximal projection of 3D movie. Time is in h:min after induction of differentiation. B) Peripheral localisation of high Rad51 cells in multicellular aggregates. The bottom panels show controls, with unlabelled wild-type cells spiked with 1% of cells expressing Neon from the *act5* gene. Images are maximal projections of 3D stacks of the mound stage of development. Scale bar is 100 μm. C) Schematic showing the subdivision of a

mound into shells of equal areas, for image quantification. D) Quantification of the distribution of high Rad51 expressing cells into the inner and outer regions (n=47 aggregates; 6 independent experiments). Controls are 1% spike-ins of *act5*-Neon (n=32; 2 experiments) or *act5*-GFP (n=39; 3 experiments) into wild-type cells (p = 4.7 x 10^{-7} and 6.1 x 10^{-10} compared to Neon and GFP, respectively). E) High Rad51 cells can be dynamic in aggregates. Images are maximal projections from a 3D movie showing switching of high expressers from outside to in. Scale bar is 100 μm. Time is in h:min after induction of differentiation.

B

$$A_{rear} = A_{mid2} = A_{mid1} = A_{front}$$

C

Rad51-Neon

rad51-Neon^{GR}

act5-Neon
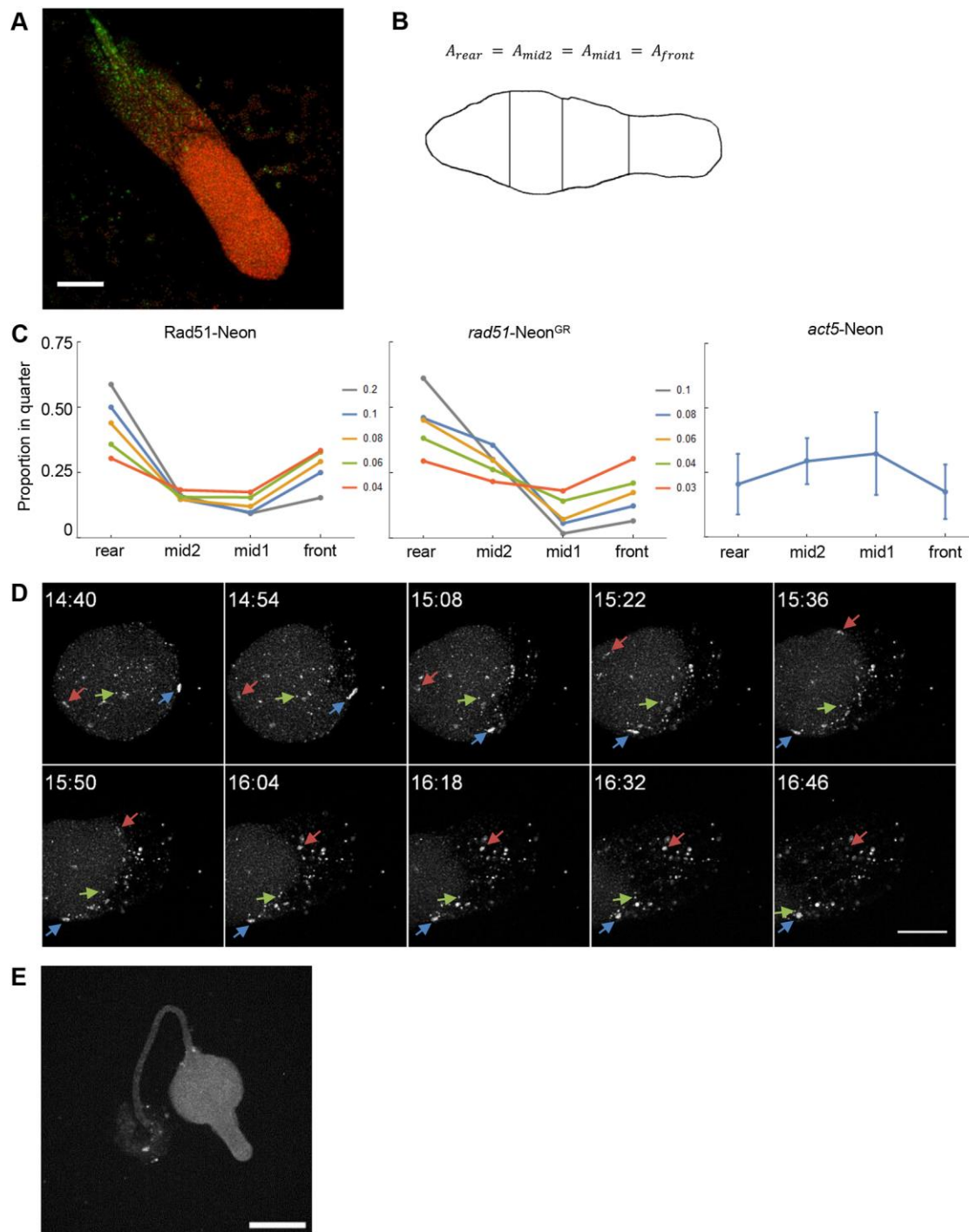
Fig. 4.

Shedding of cells undergoing spontaneous DNA damage.

A) Image of a slug showing rear localisation of high Rad51-Neon expressing cells. Nuclei are shown, for all cells, in red, with Rad51-Neon expression in green. Image is a maximal projection of a 3D stack. Scale bar is 100 μm. Additional images are shown in Fig. S5B. B) For image analysis, maximal projections of slugs were divided into 4

identical areas. C) Preferential localisation of high Rad51 cells to the rear of slugs. For unbiased determination of detection thresholds, we selected a range of thresholds (see Materials and Methods). At the most selective threshold (0.2, grey) only the extremely bright cells were detected, whereas at the lowest thresholds, weaker expressing cells are detected. The higher thresholds reveal a greater degree of localisation to the slug rear. Data are shown for Rad51-Neon cells (28 slugs; 3 experiments), a cell line where Neon replaces the Rad51 coding sequence (*rad51*-Neon[GR]; 10 slugs from 2 experiments) and a control mix of 1% *act5*-Neon cells in 99% unlabelled wild-types (11 slugs from 2 experiments). Error bars have been omitted from the Rad51 and *rad51*-Neon[GR] data for clarity- statistics are presented in the text. The error bars for the *act5*-Neon control reflect the SD of the pooled data. For Rad51-Neon, p=3.3 x 10^{-8} and 2.7 x 10^{-9} for the highest two thresholds, comparing "rear" and "mid1" sectors. For *rad51*-Neon[GR], p=3.6 x 10^{-4} and p=0.0012 for the highest two thresholds. D) Movie sequence showing shedding of high Rad51 cells as an aggregate begins to move away as a slug. See also Movies 3 and 4. Arrows show example bright cells as they are left behind. Scale bar is 100 μm. Time is in h:min after induction of differentiation. E) Exclusion of high Rad51 cells from the spore head in *Dictyostelium* fruiting bodies. 35 fruiting bodies, from three independent experiments, were analysed. 27/35 structures showed a similar pattern, while eight structures had no high Rad51 cells. Scale bar is 150 μm.
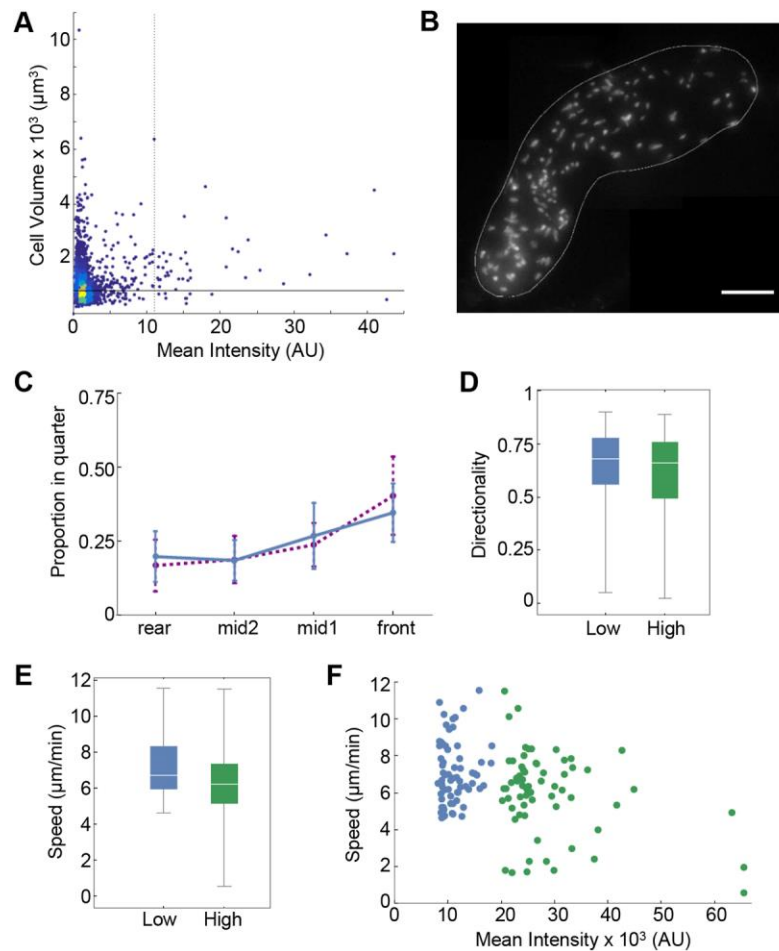
Fig. 5.

Effects of cell size and motility on development of high Rad51 cells.

A) High Rad51 expressing cells have a higher volume than the cell population average. Cell volume is plotted against the mean Rad51-Neon intensity. Each dot represents a cell. Vertical line marks the upper percentile (1% highest expressing cells) and the horizontal line marks the median. Volumes of 4742 cells from three experiments were analysed. Lighter colours refer to higher densities of data points. B) Diploid cells are not shed from the rear of haploid slugs. Slugs were developed from mixes of 0.5% mNeonGreen/mScarlet diploids mixed with 99.5% of mNeonGreen haploids. Image are maximal projections of 3D stacks of structures, with the mScarlet shown. Scale bar 100 μm. C) Preferential localisation of diploid cells to the front of slugs. 26 slugs were analysed in total. Two cell mixes were used, allowing independent clones of both diploids and haploids to be tested, with 2 biological replicates of each mix. Different

clone mixes shown in different colours. The error bars reflect SD of the pooled replicates. D-F) Quantification of chemotaxis behaviour of cells with spontaneous DNA damage. For control cells, one low Rad51-Neon cell was selected from each high Rad51-Neon cell's neighbourhood (See Fig. S6B). A total of 132 cells were analysed (66 each of high and low). D) Directionality measurements for high (green) and low Rad51 (blue) cells during early cell aggregation. For accurate estimates of directionality, we included only tracks of >10 min. No significant difference was observed in directionality between high and low Rad51 cells (p=0.230). Directionality measured as a ratio of displacement to total distance travelled. E) Cells with spontaneous DNA damage had lower speed than low expressers (p=0.015). F) The lower median speed results from a barely motile subpopulation of high-Rad51 cells. For D-F, 3 biological replicates, each with 7 fields of view were analysed.
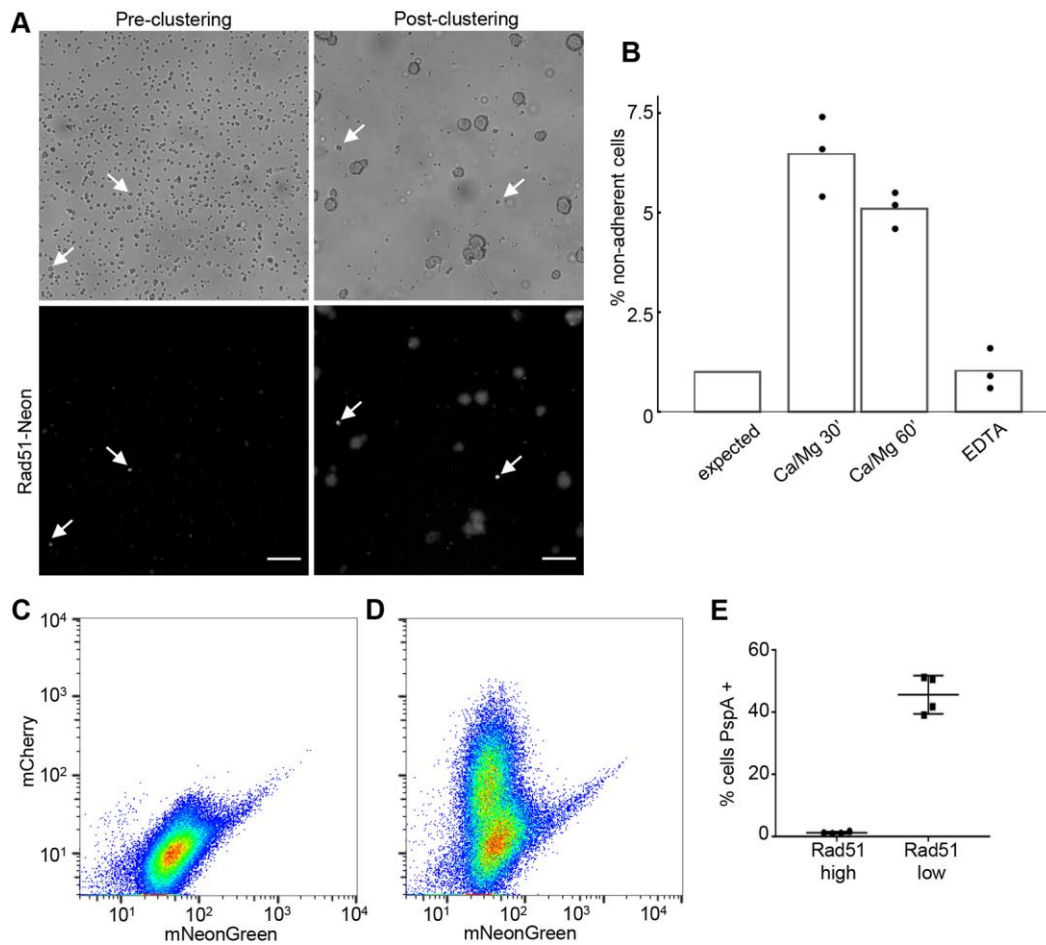
Fig. 6

High Rad51 cells are defective in cell-cell adhesion and spore differentiation

A) Reduced adhesion of high Rad51 cells. The images show disaggregated 14h developed cells directly after disaggregation (left) and after 1 h reaggregation (right). High Rad51 cells are indicated by arrows. Scale bar 100 μm. B) Quantification of the adhesion defect of high Rad51 cells. Bar chart showing the percentage of singletons and doublets that are high Rad51 after the re-aggregation of disaggregated mounds. The expected percentage of 1% corresponds to the specified detection threshold. Data are shown for re-aggregation for 30 min and 1h in 1 mM $CaCl_2$ + 1 mM $MgCl_2$, or in the presence of 15 mM EDTA for 1 h. Data points for 3 independent replicates are shown. For divalent cations, χ^2 p < 0.0001, for all replicas and timepoints, with 1537 non-adherent cells counted on average, per replicate, for post-aggregation estimates. C) Flow cytometry of Rad51-Neon cells (control). D) Flow cytometry of Rad51-Neon cells transformed with a prespore reporter plasmid (*pspA*-mCherry). Only the low Rad51-

Neon cells showed strong fluorescence in the red channel (χ^2 test: p < 0.00001). E) Impaired induction of *pspA*-mCherry in high Rad51 cells. Data show percentage of cells that are *pspA* positive, from 4 separate biological replicates. The threshold between high and low Rad51 was set at 1%. The threshold for calling mCherry positive was set based upon the control plot in C. The effects were consistent regardless of threshold chosen. See Fig. S8A for details.
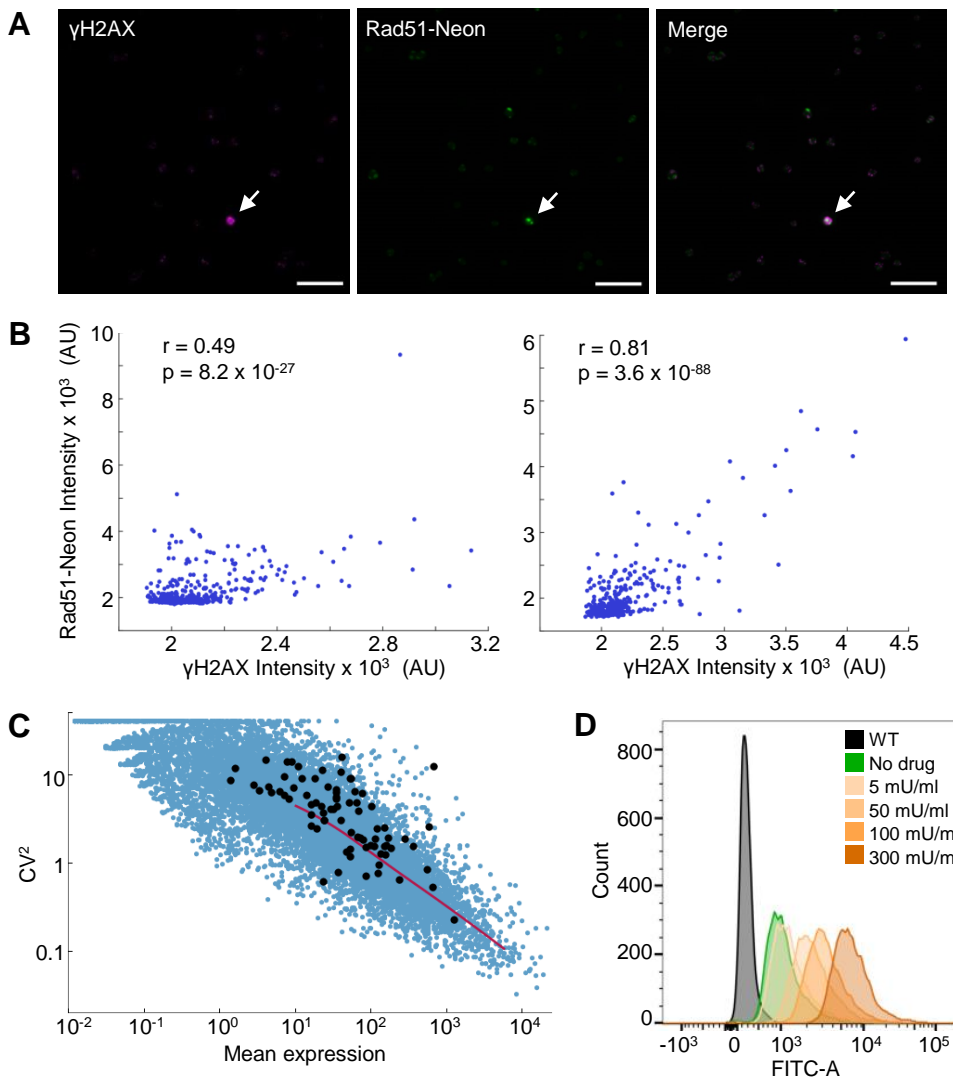
Fig. S1. Rad51-Neon as a marker for spontaneous DNA damage.
(A) Immuno-staining of Rad51-Neon cells with antibody against phosphorylated histone H2AX, which gives an enriched signal in cells undergoing DNA damage. Cells were not treated with any DNA damaging agents, so antibody staining marks out cells that have suffered spontaneous damage. Scale bar is 20 μm. (B) Correlations between phosphorylated histone H2AX staining and Rad51-Neon levels. These plots are two experimental repeats of the plot in Fig. 2A. Left: r=0.49, p=8.2 x 10^{-27}; right: r=0.81, p=3.6 x 10^{-88}. (C) Variability of GO annotated DNA repair genes in undifferentiated Dictyostelium cells. Plot shows the relationship between mean expression (read counts) and variability (CV2 – the squared coefficient of variation) for individual genes. Each gene is represented as a dot, with the red line showing a running median through the cloud of points. DNA repair genes shown in black. Genes above the line are more variable than average. and genes below the line are less variable than average. Data from Antolovic et al. (2017). (D) Flow cytometry data showing the scaling of bleomycin dose to induction of Rad51-Neon expression (one of two biological replicates shown).
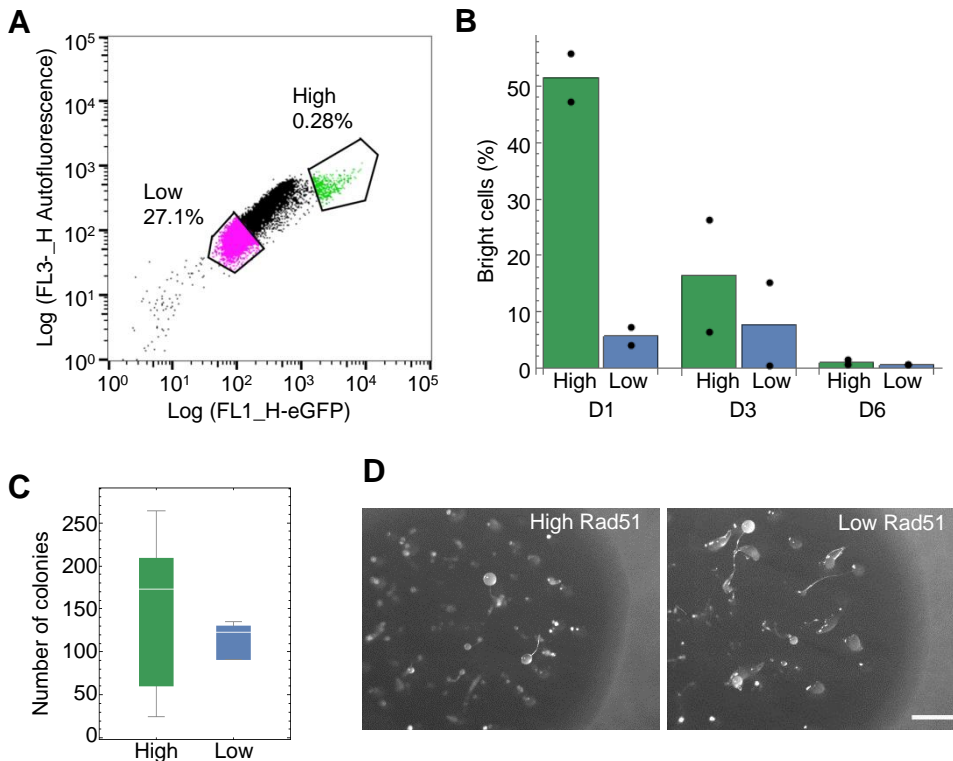
Fig. S2. Long term monitoring of Rad51 expression and the effects of spontaneous DNA damage on cell viability.

(A) Plot showing the population fractions isolated by FACS for measuring clone forming potential and long-term developmental prognosis. (B) Dynamics of the proportion of high cells, 1 day, 3 days and 6 days after purification of high and low cells by FACS. Cells were assigned to high or low Rad51 using fluorescence microscopy. The low cells show a temporary induction in a small proportion of the population after FACS. Black dots represent values from each of 2 replicates. To assign cells to high or low, an intensity threshold was imposed by eye on a non-sorted population of 2569 Rad51-Neon cells, with the imposed threshold categorising the percentage of bright cells as 0.93%. (C) Clone forming potential of high and low Rad51-Neon cells. Data shows the number of clones recovered, on bacterial growth plates of 150 FACS-sorted high and low Rad51-Neon cells. Data are combined from 5 independent experiments (p=0.68). (D) Example images from the 5 biological replicates showing long term developmental potential of single cell clones derived from high and low Rad51 cells is similar.
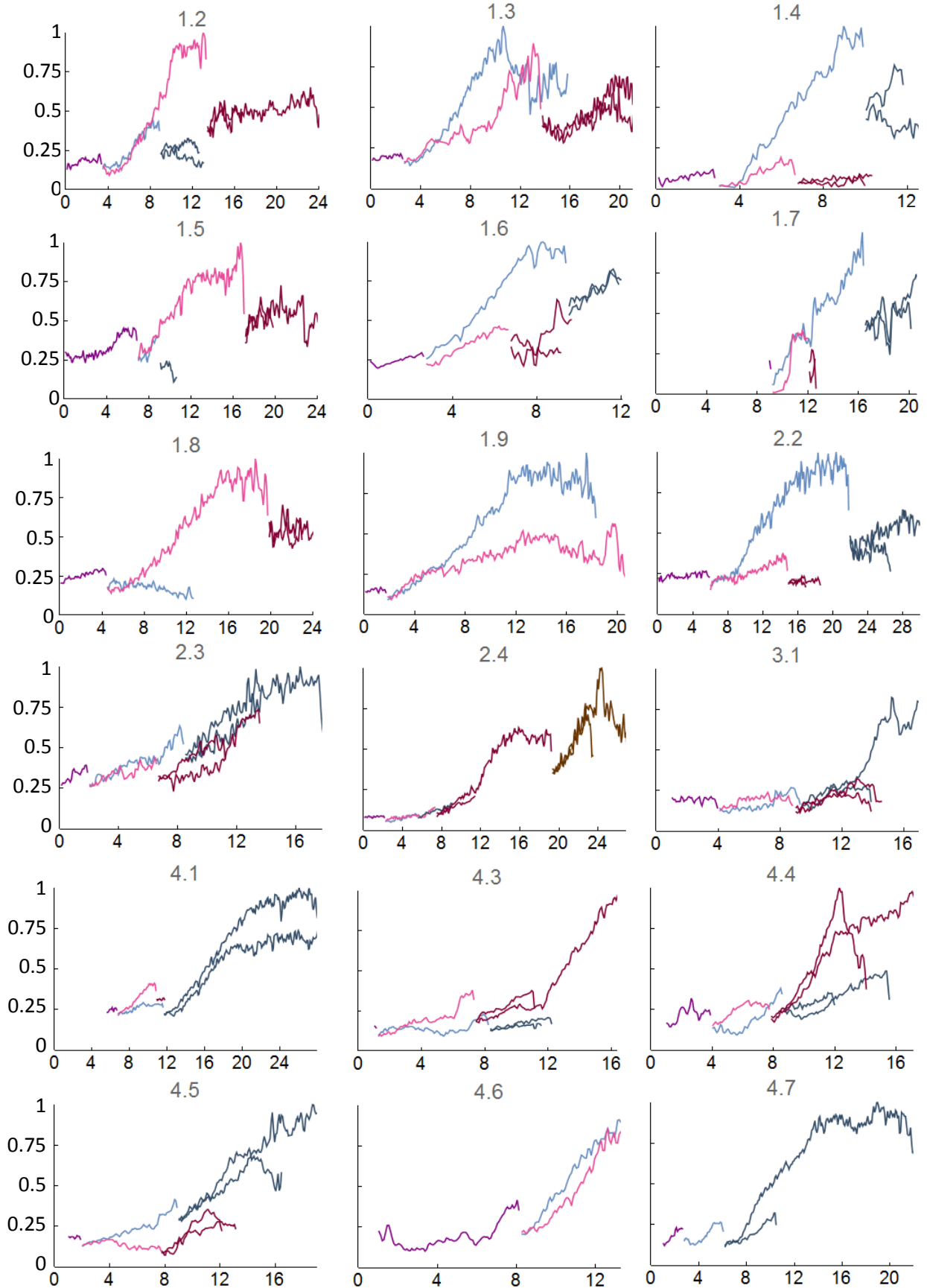
Fig. S3. Time lapse imaging of spontaneous Rad51-Neon induction.
Individual panels show intergenerational Rad51 expression dynamics for 18 cell lineages where the complete process of induction was captured from multi-generation time lapse movies of several thousands of cells over 4 independent imaging experiments. This is the expanded dataset relating to Fig. 2D.

A

B
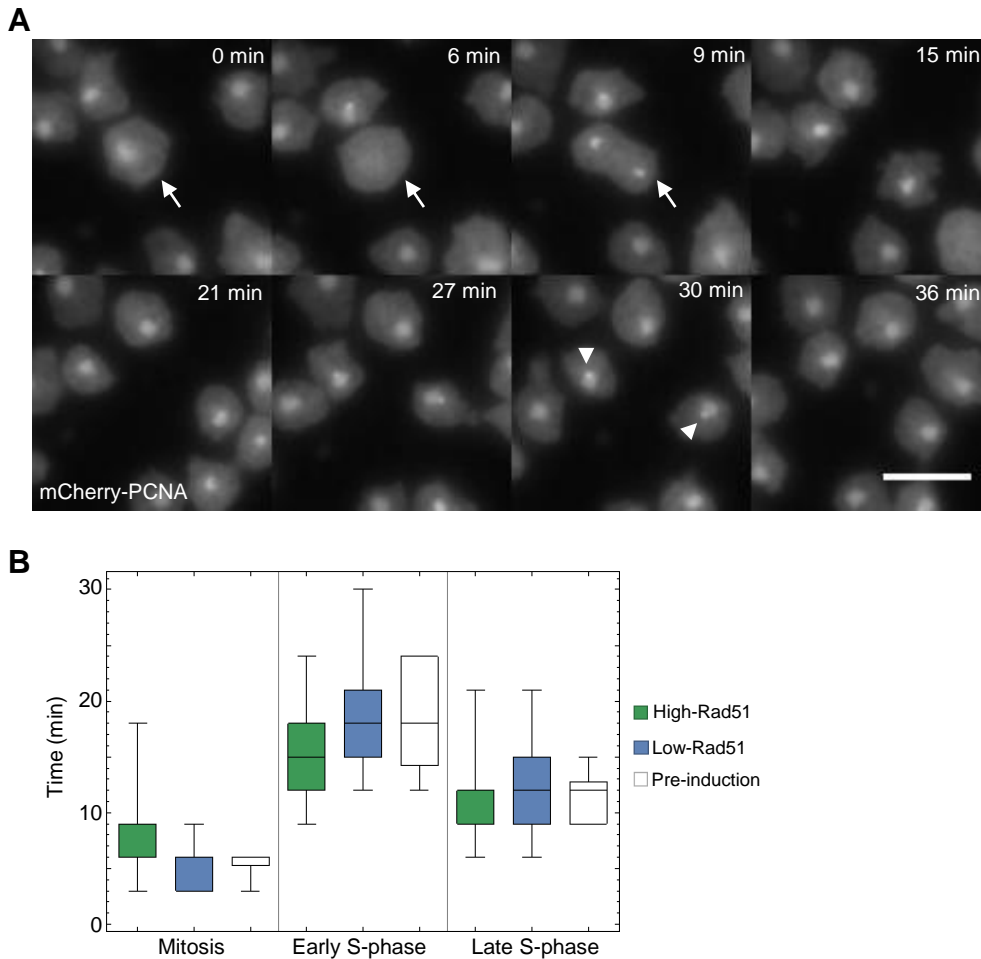
Fig. S4. Delineating cell cycle phases using mCherry-PCNA.

(A) Upon mitotic entry, nuclear PCNA is dispersed throughout the cell (6 min), before rapidly being recruited back to chromatin upon the onset of division (arrows: 0, 6 and 9 min). There is no G1, with cells immediately commencing early S-phase. The end of early S-phase and the beginning of late S-phase are marked with the appearance of large PCNA foci corresponding to the replication of heterochromatin (arrowheads, 30 min). Scale bar 15 μm. (B) The plot shows the durations of the various cell cycle phases for high and low Rad51-Neon cells, and cells prior to Rad51 induction ("pre-induction"), with data pooled from 4 independent replicates. High cells have slightly longer mitoses (p=0.0013, n=36 (high) and n=57 (low)), slightly shorter early S-phases (p<0.0001, n=65 (high) and n=108 (low)) and no significant change in their late S-phase durations (p=0.073, n=64 (high) and n=104 (low)). The rare cells (n=5) that could be tracked for their entire cell cycle before Rad51-Neon induction (pre-induction) showed no clear perturbation of M and S-phase durations.
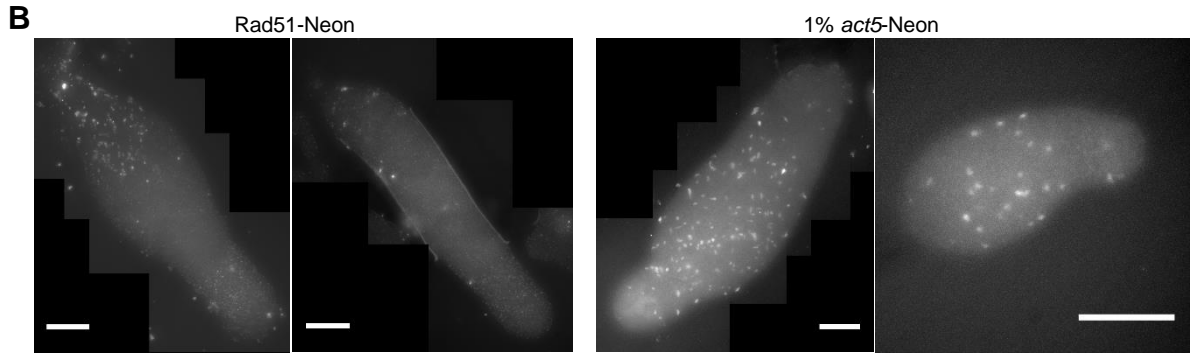
A

B

Rad51-Neon   1% *act5*-Neon

C

Rad51-Neon   EtBr

r = 0.05
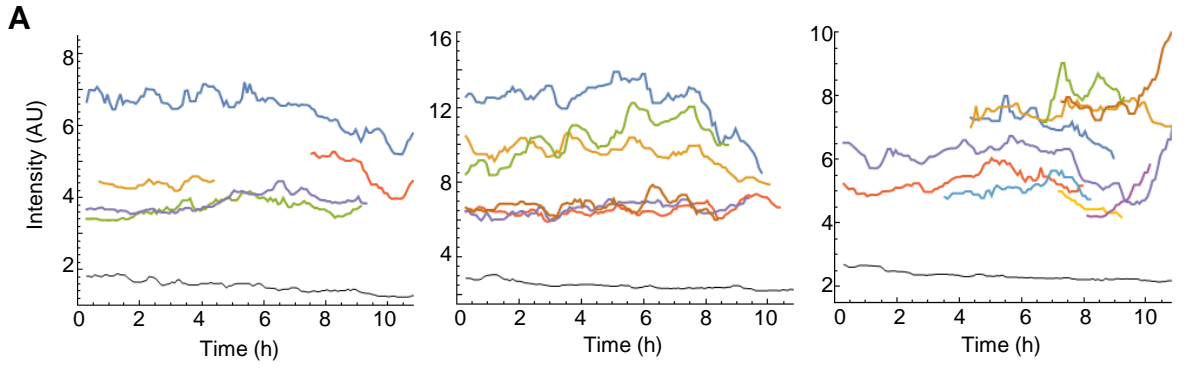p = 0.35

D
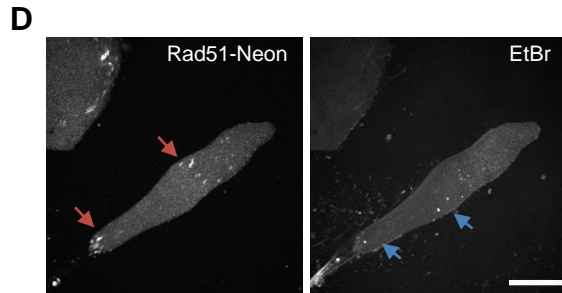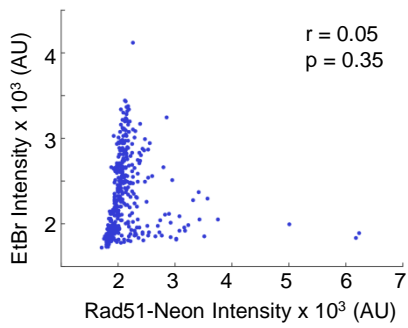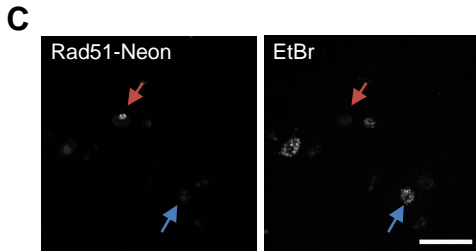
Rad51-Neon   EtBr

Fig. S5. Developmental fates of cells undergoing DNA damage.

(A) No large scale expression changes of high Rad51-Neon cells during early development. Examples of intensity fluctuations of Rad51-Neon during pre-aggregative development. Lines show intensity traces of individual developing Rad51-Neon cells, smoothed with a running median of 6 frames (30 minutes). Cells were tracked until they reached multicellular structures, at which point the fluorescence increased due to convolution effects. The black line at the bottom of the plot shows the fluctuations of the background signal, taken from an area of the field of view without cells. Each plot is a different field-of-view. No strong increases were observed post starvation onset in 6 independent replicates. (B) Examples of slugs generated during development of Rad51-Neon cells (left) and control mixes, with wild-type cells spiked with 1% *act5*-Neon cells (right). Scale bars are 100 μm. Relates to Fig. 4A-C. (C,D) High Rad51-Neon cells do not become Sentinel cells. (C) Staining of cells from disaggregated slugs with ethidium bromide (which labels Sentinel cells), with the plot showing no correlation between Rad51-Neon and ethidium bromide staining (r=0.05, p=0.35). Typical data from 3 independent experiments. (D) A comparison of ethidium bromide staining and Rad51-Neon in intact slugs. Typical data from 3 independent experiments.
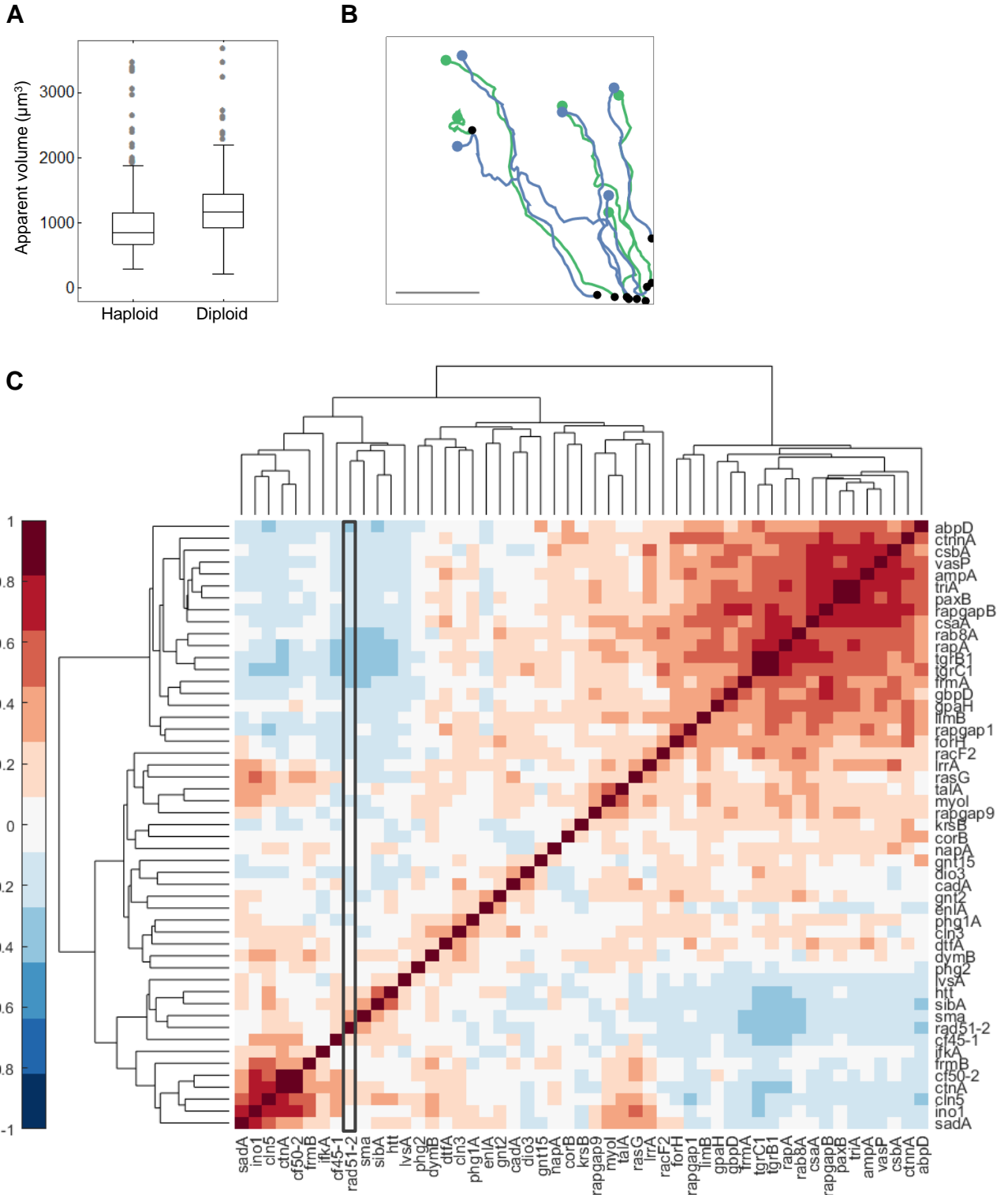
Fig. S6. Measuring cell size, motility and adhesion potential.

(A) Diploid cells have a higher volume than haploid cells. The experiment shown is a representative experiment of 4 replicates. Total of 246 haploid and 232 diploid cells were measured (p=7.2 x 10^{-13}). Related to Fig. 5B,C. (B) Example cell tracks of aggregating *Dictyostelium* cells within a single field of view (relates to Fig. 5D-F). High Rad51-Neon cell tracks are marked in green and low expressers in blue, with the initial position marked as a dot in the same colour and the track endpoint marked as a black dot. Scale bar 100 μm. (C) Heatmap showing correlations between *rad51* expression and genes with GO-annotated roles in adhesion and an associated adhesion phenotype. Correlation values are taken from single cell transcriptomics data of *Dictyostelium* mounds at 14 h of development (Antolovic et al., 2019). The black rectangle highlights the correlations with *rad51.*
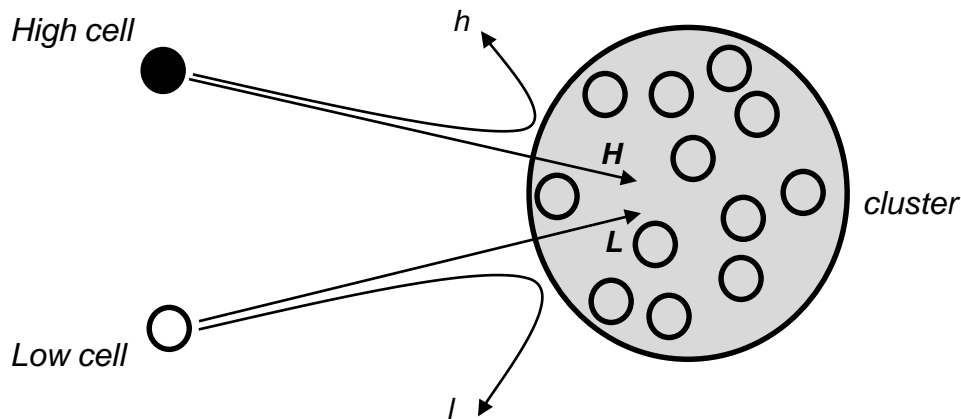
Fig. S7. Estimation of the relative likelihood of damaged and non-damaged cells to remain non-adherent during cell cohesion assays.

Let the number of high and low cells entering a cluster be H and L, respectively. Let the number of high and low cells rejected from a cluster be h and l, respectively. The probability that a high cell will be rejected from a cluster is $P_h = \frac{h}{h+H}$ and the probability that a low cell will be rejected from a cluster is $P_l = \frac{l}{l+L}$. The relative probabilities of high and low cells being rejected from a cluster are therefore: $\frac{P_h}{P_l} = \frac{h}{l} \times \frac{l+L}{h+H}$. In our case $\frac{l+L}{h+H} = 99$. In the presence of divalent cations $\frac{h}{l} \approx \frac{5}{95}$, therefore $\frac{P_h}{P_l} \approx 5.2$. In the absence of divalent cations $\frac{h}{l} \approx \frac{1}{99}$, therefore $\frac{P_h}{P_l} \approx 1$.
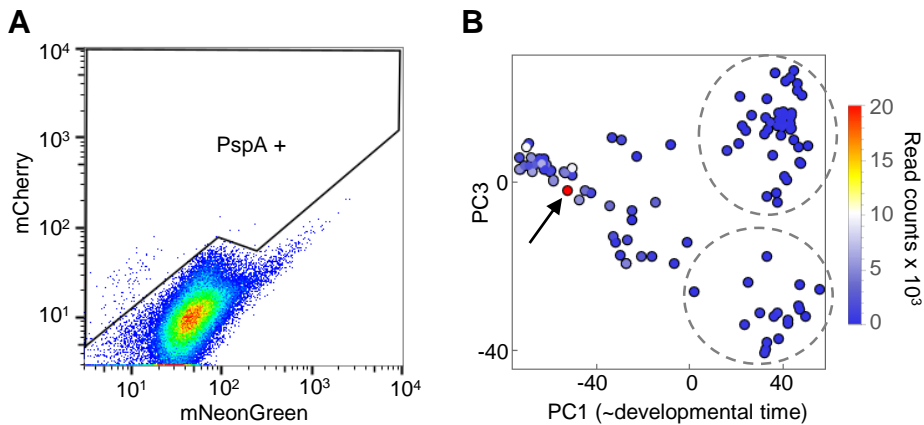
Fig. S8. Developmental gene expression of high *rad51* cells.
(A) Setting the threshold for calling *pspA*-mCherry expression. Data show a flow
cytometry plot of the Rad51-Neon cell line. The data are the same as in Fig. 6C, but
overlaid with a line demarcating the specified cut off. Different selected thresholds
did not alter the conclusion that high Rad51-Neon cells poorly induce mCherry
from this prespore promoter. (B) Principal component analysis of single cell
transcriptomic data from *Dictyostelium* mounds (Antolovic et al., 2019) coloured to
show single cell levels of *rad51* mRNA. PC1 is a proxy for developmental time, with
cells on the right more advanced in development. At least one cell (arrow) showed
expression comparable to the undifferentiated high *rad51* cells, and this cell
clustered with cells that have not showed selection of the spore (top cluster circled)
or stalk fates (bottom circled cluster). These data imply that high *rad51* cells, in
addition to becoming aggregation competent, can advance their gene expression at
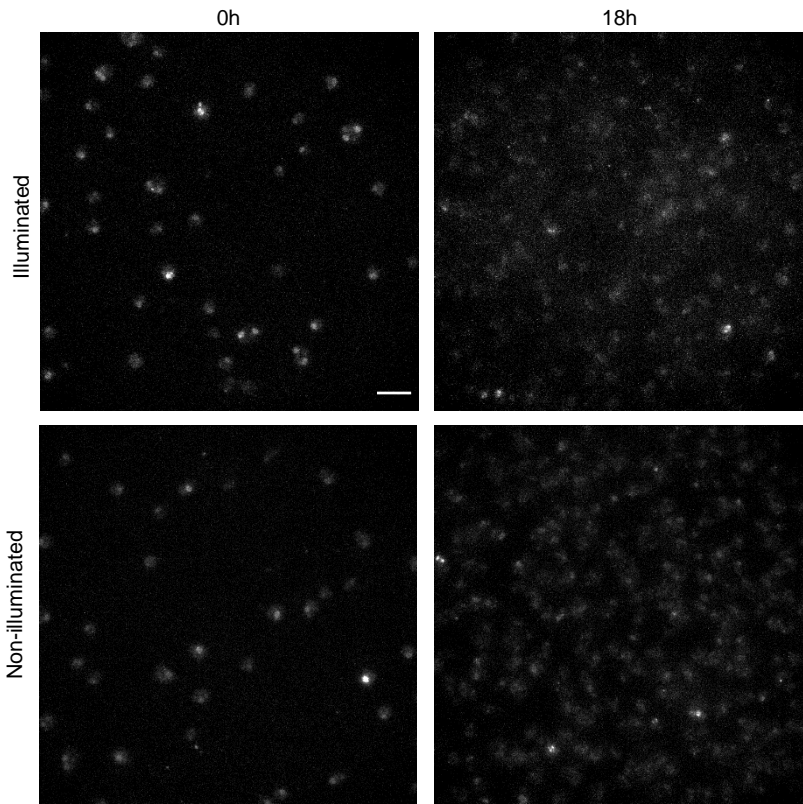least to a state just prior to overt fate selection.

**Fig. S9. Standard imaging protocols do not induce Rad51-Neon expression.**
Panels show images of fields captured on the wide field imaging set up used for the cell cycle phase analysis. The images show a field of view at the onset and end of an 18 h 3D time lapse with a frame interval of 2 min, and 20 z slices per field of view per time interval. The distribution of Rad51-Neon intensities is the same for samples illuminated using this protocol, and those for which the above images were the only ones captured. Scale bar 20 μm.

Table S1. Genes highly correlated in their expression to *rad51.* We searched for genes with a read out in the single cell transcriptomics of greater than 10 that had a correlation value, r, greater than 0.5. Of the 30 genes passing this cut-off, 26 are involved in DNA repair and/or replication.

Click here to Download Table S1
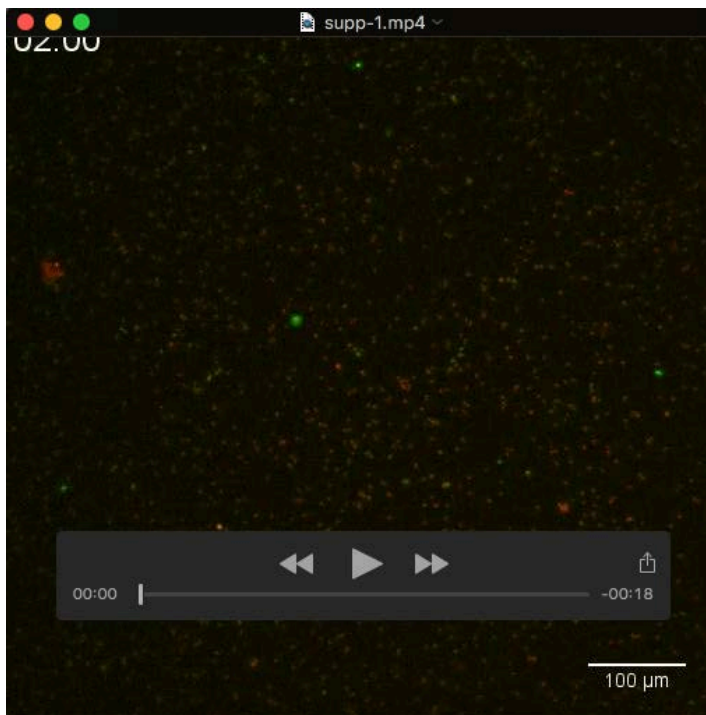
Movie 1. Time-lapse imaging of *Dictyostelium* aggregation showing the behaviour of cells with spontaneous DNA damage. High Rad51-Neon expressing cells can be tracked from the onset of differentiation, until late aggregation and slug departure. The high Rad51 cells appear to remain at the edge of cell aggregates. All cells express the red nuclear marker (H2Bv3-mCherry). Time after starvation onset is shown.
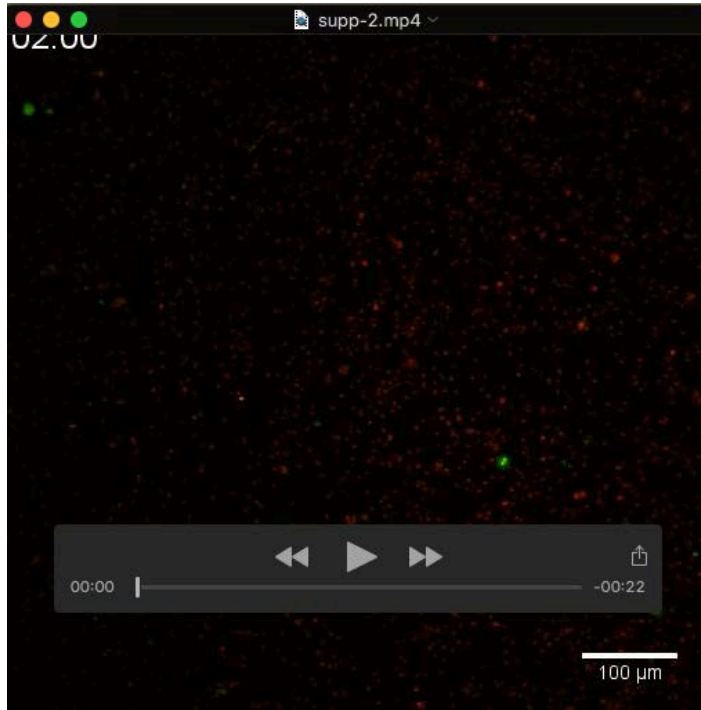
Movie 2. Time-lapse imaging of *Dictyostelium* aggregation showing the behaviour of cells with spontaneous DNA damage. Alternative movie to Movie 1. Time after starvation onset is shown.
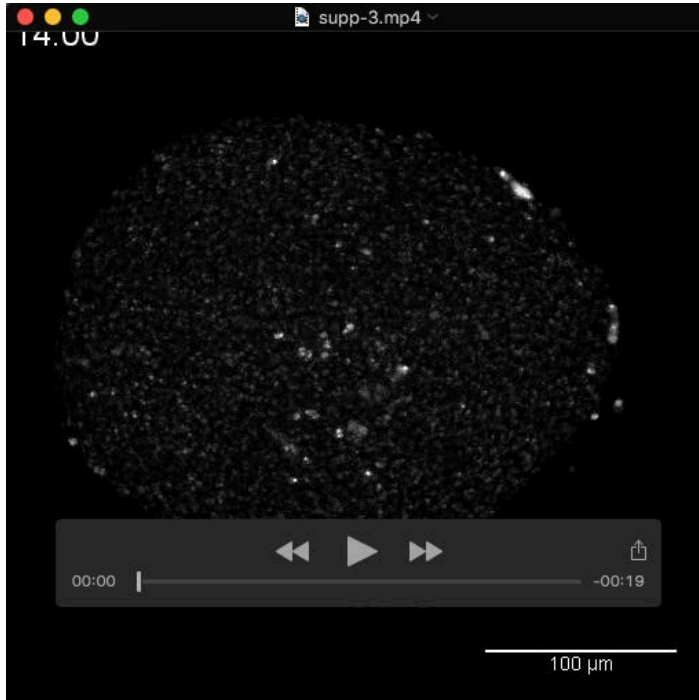
Movie 3. Movie showing shedding of high Rad51 cells as an aggregate begins to move away as a slug. Time after starvation onset is shown.
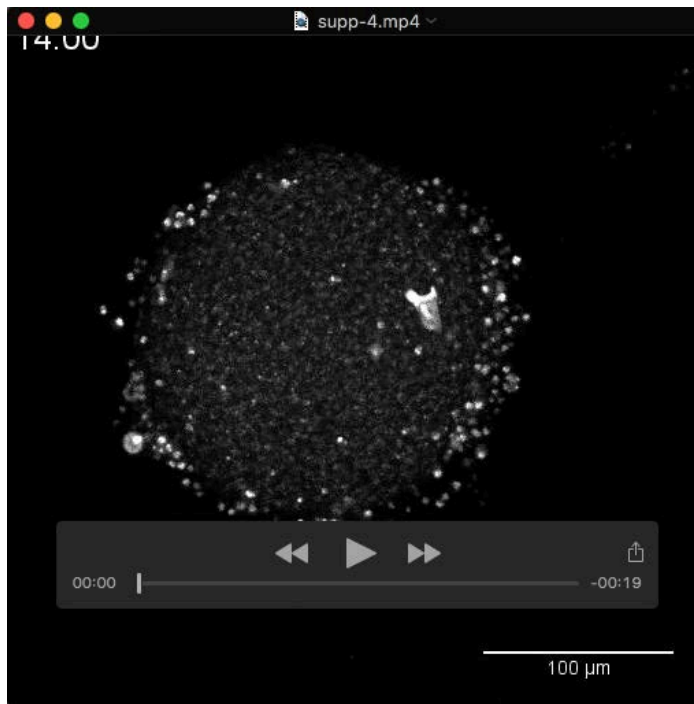
Movie 4. Movie showing shedding of high Rad51 cells as an aggregate begins to move away as a slug. Alternative movie to Movie 3. Time after starvation onset is shown.